

REU 2016



Research Experience for Undergraduates

Section 2

Support for the REU program is provided by the NSF MRSEC program (DMR-1120296) and the REU Site program (DMR-1460428).

TABLE OF CONTENTS

REU	Faculty Advisor	Page
Hebner, Tayler	Prof. Lena Fitting Kourkoutis	03
Overly, Emma	Prof. Tobias Hanrath	08
Pruiksma, Tylar	Prof. Lawrence Bonassar	15
Rosch, Kelly	Prof. Henning Lin	23
Vazquez, Julio	Prof. Brian Kirby	28
Xie, Yanyou	Prof. Peng Chen	39
Zamora-Marin, Geraldine	Prof. Gregory Fuchs	44
Zhang, Irene	Prof. Gregory Fuchs	54
Zhelyskova, Vesta	Prof. Christopher Xu	61

Revealing the Nanoscale Structure of Porous Silicon using Electron Microscopy

Taylor S. Hebner

Department of Chemical Engineering, University of Minnesota Duluth, Duluth, MN

Jade M. Noble

Robert Frederick Smith School of Chemical and Biomolecular Engineering, Cornell University, Ithaca, NY

Lena F. Kourkoutis

School of Applied and Engineering Physics, Cornell University, Ithaca, NY
Kavli Institute at Cornell for Nanoscale Science, Ithaca, NY

In order to investigate the nanoscale structure of porous silicon, scanning transmission electron microscopy (STEM) can be used to obtain high resolution images of the material. For STEM imaging to be effective, the specimen to be imaged must be prepared to a thickness of 200 nm or less. If not inherently electron-transparent, the sample can be thinned through the processing technique of polishing. If polishing is unsuccessful, a more robust technique, such as focused ion beam milling, can be utilized. With an amenable sample and user expertise, both techniques can produce samples that can be used in STEM and result in high-resolution imaging conditions that reveal the nanoscale structure of the porous-Si.

1. INTRODUCTION

Porous silicon is a very unique material that can be used to model intricate systems, such as the effect of aerosols on cloud formation caused by impurities in airplane exhaust acting as nucleation centers. In this example, the porous Si serves as a template for the freezing transition of supercooled liquids. To better understand the freezing kinetics within porous Si, its complex pore structure must be examined. The pores, ranging from 2nm to 10nm in diameter, must be investigated with a technique capable of single-nanometer resolution. With its ability to image materials with angstrom resolution, scanning transmission electron microscopy (STEM) is an ideal method for probing the nanoscale structure of porous silicon.

Electron microscopy is a powerful tool for imaging materials at high resolution. In STEM, images can even be obtained at atomic resolution, as shown in Figure 1.

In STEM, a beam of electrons is focused to a small probe that scans across the surface of the

specimen. These electrons pass through the sample and are scattered at different angles based on the atomic number of the atoms in the sample. A detector then collects the scattered electrons and forms an image with contrast that varies by element. In annular dark field imaging, heavier elements present in the sample appear brighter in the final image [1]. This is diagrammed in Figure 2. If the sample being imaged is not thin enough, the electrons will not

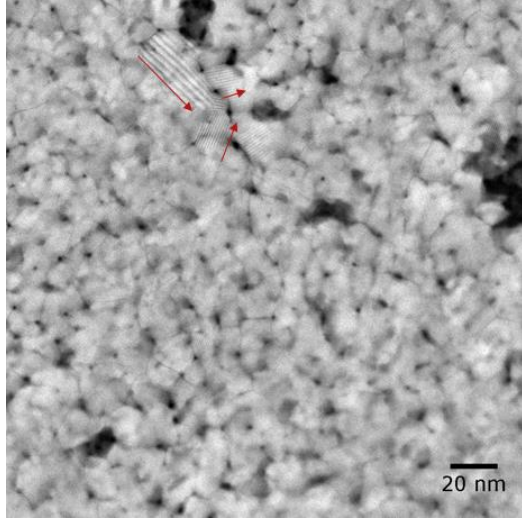


FIG 1. STEM image of a gold-coated grid. Atomic lattice moiré fringes are indicated by red arrows.

be able to pass through, therefore resulting in poor image quality or even no image at all. In STEM, the specimen being imaged must be less than 200 nanometers thick to allow electrons to be transmitted.

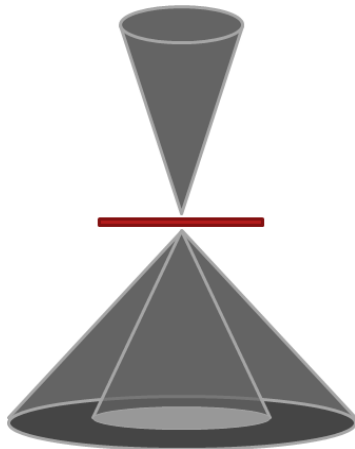


FIG 2. Representation of STEM process where electron probe scans sample, electrons pass through the sample, and a detector collects the electrons scattered at different angles.

In order to achieve the sample thickness required for STEM imaging, a technique called mechanical polishing is often used [2]. This technique is relatively inexpensive and often produces high quality samples. However, some types of samples are particularly difficult to polish, such as porous silicon. Because of its porosity (up to 70%), porous silicon has a

tendency to shatter when polished. When a sample like this proves to be nearly impossible to thin by polishing, focused ion beam (FIB) milling is used because it is a more precise, intricate form of thinning and does not apply mechanical force to the sample as polishing does [3]. This method is usually only utilized when it has been determined that polishing is ineffective.

FIB milling is reserved as a last resort for sample thinning because of its cost and time dependency. Usually, multiple attempts have been made with traditional polishing methods before determining that use of the FIB is necessary. However, if this technique is pursued and is successful, high resolution images equivalent to those acquired with traditionally polished samples can be obtained.

Using polishing and FIB techniques, an electron-transparent sample of porous silicon can be obtained and imaged in STEM to produce an accurate high resolution representation of its pore structure, which can in turn be used to develop the appropriate kinetic and thermodynamic models that best describe the transition dynamics from supercooled liquids to ice.

2. METHODS

2.1 Polishing

A sample of porous silicon of approximately 2 mm width and length is used for polishing. The sample is soaked in heated ethanol for 5 minutes, followed by heated methanol for 5 minutes to clean the sample. The ethanol and methanol are heated in petri dishes on a hot plate to just below the boiling point of ethanol (79.29°C)[4]. Once cleaned, the sample is observed in an optical microscope. Residue remaining on the surface is removed with a cotton swab soaked in methanol. Once cleaned, the sample is attached to an optical flat. The optical flat is heated on a hot plate at 400°F. A small amount of wax is then melted onto the straight edge of the top of the optical flat. While the wax is still hot, the sample is placed film-side down into the wax, with one edge lining up with the straight edge of the optical flat. The film side is positioned on the wax because the region of interest is located right beneath the film, and we want to polish away the rest of the sample, leaving only the porous layer in the final sample.

The optical flat and porous-Si are then set aside to cool until wax hardened.

While the optical flat cools, the polisher (Allied MultiPrep System) is prepared. The polishing head is set to a 4° tilt angle. A 15µm polishing paper is secured to the spinning disc with water. The optical flat with porous Si attached is then attached sample-side down to the polishing head. The polishing paper is spun in a clockwise direction at 50 rpm. The paper is sprayed with BlueLube (Allied) and the polishing head is lowered so the sample makes contact with the spinning paper. As the sample is being polished, residue on the polishing paper is removed by holding a Kimwipe™ in front of the sample. The paper was sprayed every 5-10 seconds with BlueLube to ensure smooth and clean polishing. The porous-Si is polished with a 15µm paper until the thinnest edge measures 250µm with a Mitutoyo pressure thickness gauge. When polishing, the thickness is only measured with the pressure gauge down to 150µm due to the fragility of thinner regions. The 15µm paper is then replaced with a 6µm paper and the polishing process is repeated until the porous-Si is 150µm thick. The 6µm paper is then replaced with a 3µm paper and the sample is polished until the trail left by the porous-Si on the polishing pad becomes wider and the edge of the optical flat is beginning to be polished. The 3µm paper is then replaced with a 1µm paper and the porous-Si is polished for approximately 30 seconds. The sample was then observed under an optical microscope. If optical fringes are not observed at the edge of the porous-Si, it is reattached to the polishing head and polished for 10-20 seconds longer and observed again. This is repeated until optical fringes, which indicate electron transparency, were observed. The optical flat is then set sample-side down onto a filter paper in a petri dish of ethanol on the hot plate. The optical flat is tilted so that when the wax dissolved, the sample falls onto the filter paper. Once the sample falls off, it is transferred on the filter paper into the methanol and allowed to sit in methanol for 5 minutes. The filter paper and porous-Si are then allowed to dry.

Once the sample is dry, a 3mm molybdenum STEM grid is prepared. A small amount of M-Bond™ is placed on the edge of the grid hole with the end of a toothpick that has been thinned

with a razor blade. The thick side of the porous-Si wedge is attached film-side down to the m-bond. The grid is then placed on a hot plate at 400°F for 5 minutes or until m-bond is set and sample is ready to be stored or imaged.

2.2 Focused Ion Beam (FIB) Milling

The porous-Si often cracked under the mechanical stress of the polishing process, so sample preparation for FIB was considered. A sample of approximately 2mm width and length is used. This sample is first polished at a 4° angle using the polishing techniques described above for 15µm and 6µm papers. The sample is then thinned with 3µm paper to approximately 15-20µm, as determined by the amount polished away according to the thickness gauge on the polishing head. This is done to reduce time required to thin in the FIB. The porous-Si was then removed from the optical flat and attached to a grid using procedure described above.

The grid and thinned porous-Si are loaded into the FEI Strata 400 FIB-SEM dual beam setup such that the area of interest was perpendicular to the beam direction, with the thin side directed away from the beam. The ion gun was oriented with the sample as shown in Figure 3. The sample is then milled with Ga⁺ ions at 3kV and 5.0 mA until a thin region is observed in the SEM view of the FIB mechanism. A final milling stage is then performed at 1.0kV and 5.0 mA to smooth the surface to be imaged. Once thinned, the sample is removed from the FIB and stored or imaged.

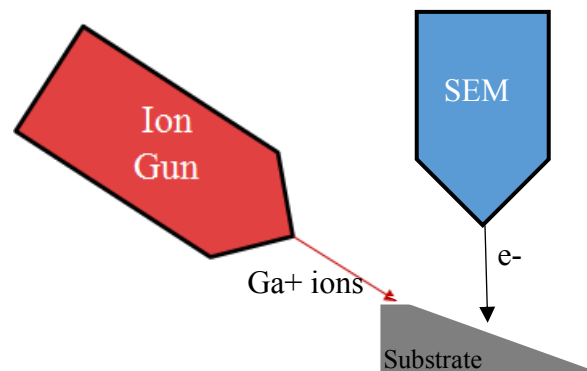


FIG 3: Representation of FIB process where gallium ions mill away the substrate, leaving a wedge with an electron-transparent edge.

2.3 STEM Imaging

The polished porous-Si samples prepared by the polishing and FIB techniques were imaged by an FEI Titan Themis aberration-corrected STEM microscope at an acceleration voltage of 120 kV. Images were collected at 28,500x, 57kx, 115kx, 225kx, 640kx, and 910kx.

3. DISCUSSION

3.1 Polishing

This method of sample thinning was successful for one sample of porous Si. Since each sample may have different physical properties, it is important to note that portions of the methods, such as time spent on each polishing paper or amount of wax used, may have varied slightly depending on the sample. Once using the 3 μ m and 1 μ m papers, it was helpful to periodically observe the sample in an optical microscope to check for any cracking or chipping, which occurred frequently with porous Si. If a sample was polished successfully, optical fringes can easily be seen at the edge of the electron transparent substrate, as shown in Figure 4. In the case of porous Si, the sample was prone to shattering on the optical flat before optical fringes were visible.

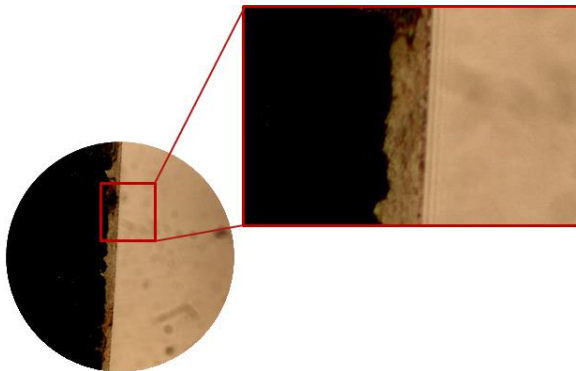


FIG 4: Optical fringes can be seen on the edge of the sample, indicating electron transparency.

3.2 Focused Ion Beam Milling

In the case of porous Si, the sample was generally unable to be thinned using polishing due to

cracking of the porous layer. In preparation for FIB, it also proved to be a challenge to thin the sample to less than 20 μ m. This made using the FIB very difficult and time consuming, however, thinned regions on the sample were eventually achieved and subsequently imaged with STEM.

3.3 STEM Imaging of Porous Silicon

Once a sample of successfully polished porous silicon was obtained, high resolution images were produced through STEM, as shown in Figure 5. In this image, the pore structure can be clearly seen and measured. This plan view image gives details about pore distribution and size, however does not indicate how the pores propagate through the sample. In order to observe this propagation in the future, a cross-sectional sample could be imaged or tomography could be done on the sample to provide three-dimensional structural information about the pore network.

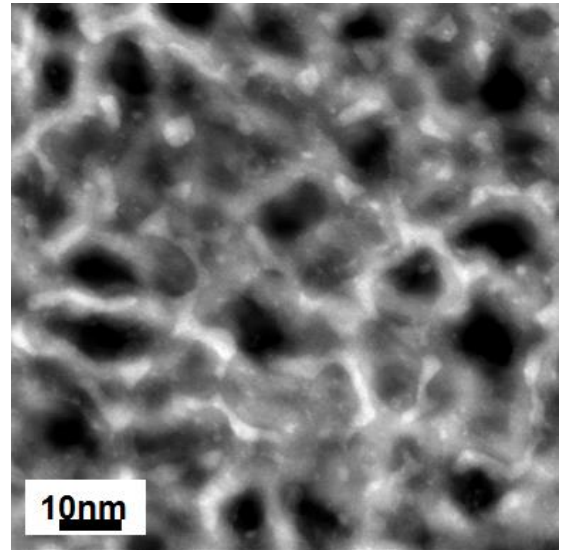


FIG 5: STEM image of successfully polished porous silicon.

4. CONCLUSIONS

Porous silicon is a complex material that can be very useful when its pore structure is understood. STEM has proven to be an effective method of obtaining high resolution images resolving the size and distribution of pores in the material. In order to use STEM to analyze this nanoscale structure, electron-transparent samples must be prepared one of two ways. Polishing is a

technique often used for thinning that can usually produce high quality samples with an electron-transparent edge. With samples that are particularly difficult to polish, focused ion beam milling is sometimes used, but with more hesitation due to the time it requires and cost of operation. Both techniques can produce samples of porous silicon can be used in STEM to produce high resolution images that allow observation of its nanoscale structure.

ACKNOWLEDGEMENTS

Support for this work was provided by the Cornell Center for Materials Research and the REU Site program (DMR-1063059) and the NSF MRSEC program (DMR-1120296). I would like to thank the CCMR facilities managers, specifically Mariena Silvestry-Ramos, Malcolm (Mick) Thomas, and John Grazul for assistance with equipment and the Kourkoutis Electron Microscopy Group, especially my mentor Jade M. Noble, for all of their help with this project.

REFERENCES

1. Nellist, P. D., and S. J. Pennycook. "The principles and interpretation of annular dark-field Z-contrast imaging." *Advances in imaging and electron physics* 113 (2000): 147-203.
2. Mukhopadhyaya, Sharmila M. In *Sample preparation techniques in analytical chemistry*; John Wiley & Sons: Hoboken, NJ, 2003; pp 377-411.
3. Mayer, J.; Giannuzzi, L. A.; Kamino, T.; Michael, J. *MRS Bull. MRS Bulletin* **2007**, 32 (05), 400-407.
4. <https://pubchem.ncbi.nlm.nih.gov/compound/ethanol#section=Boiling-Point>

Genetic Algorithm Lead Discovery of Nanoparticle Structures

Emma Overly¹, Eliad Peretz², Douglas Nevers², Tobias Hanrath²

¹Department of Chemical Engineering, Bucknell University, Lewisburg, PA.

²Department of Chemical Engineering, Cornell University, Ithaca, NY.

Abstract

Nanoparticles are at the forefront of light technologies and semiconductor technologies. Nanoparticles' optic and electronic properties are dependent on their structures. In order to take advantage of a nanoparticle's tunable properties, it is important to know the 3-D structure of the nanoparticle. But, because of nanoparticles' heterogenous structures, typical X-ray diffraction structure determination techniques aren't available. This project uses a genetic algorithm to help predict the 3-D structure of the nanoparticle. With the help of our computational model and single crystal X-ray diffraction PDF data, the structure of nanoparticles can be determined to a residual of 0.18.

I. Introduction

Seen as a prominent focus in scientific research today, nanoparticles can contribute to applications in many fields. Specifically, nanoparticles have light absorption and light emission uses seen in LED screens or solar cells. Their optic properties are strongly based on their size and structure. The larger the nanoparticle, larger the wavelength it emits or absorbs. In addition to their optic technology applications, nanoparticles are used in fields of energy technology, such as semiconductors. The draw to use nanoparticles in these fields is because of their highly tunable properties. Nanoparticles' properties are dependent on their structures, so there is a need to know what the 3-dimensional structures look like.

For crystalline homogenous structures, scattering patterns from experimental X-Ray diffraction are sufficient for structure determination. But, most nanoparticles are heterogenous and too small to fully display a sufficient scattering pattern to predict a structure. Some experimental data for nanoparticles can be obtained in the form of an atomic pair distribution function, also referred to as a PDF. This PDF data represents all interatomic distances between all atoms within the nanoparticle structure. With this information, and the help of computational modeling, structures can be predicted within some degree of accuracy. The "closeness" of the structure prediction is rated by a residual value. Which is essentially how closely the experimental PDF data matches the PDF data of the computational model. Typical residuals that have been seen in literature are between 0.1-0.2. The goal of this project was to create a computational model to predict nanoparticle structures with residual values between 0.1-0.2.

The computational model used within our research is a genetic algorithm. Genetic algorithms are used in search and optimization problems to find the "best possible" solution to a problem. Genetic algorithms are based on the natural selection process in nature: each member of a population produces a set of offspring through a crossover, some having mutations. Based on how "fit" the offspring are, a select number of offspring survive and move onto the next generation of a population. The offspring that are deemed "unfit" will not survive, and will be removed from the population for the next generation. The benefit in this is that only the fittest candidates survive a series of generations. In the context of the nanoparticle structure prediction problem at hand, genetic algorithms will be beneficial for altering structures of an initial population of candidate structures, until only the structures with the lowest residuals remain.

II. Methods

Within this methods section, the back and forth between the computational model and the experimental X-Ray diffraction PDF data will be described. The end goal in this structure prediction method will be to predict a structure with a low residual.

GA Overview

For our trials, we were predicting the structure of the Owen-tetrahedral structure (shown below in Figure 1). The Owen-tetrahedral structure was able to be fully determined using X-ray diffraction, but this is not always the case for all nanoparticles. Although the results that appear in this paper are for the Cadmium-Selenide Owen-tetrahedral, our code is dynamic and works for any nanoparticle structure prediction. We use the Owen-tetrahedral because it is a known quantity that we can compare our results to. For the beginning of our genetic algorithm, we start off with a structure guess. The guess should typically be the bulk crystal structure (Figure 1) with the correct types atoms in it. The ratio, number, and position of the atoms do not matter and will be adjusted within the genetic algorithm. Once an initial guess is chosen, a population of N candidates is generated. All the candidates are going to be similar to the initial guess that was picked, with deviations in approximately 60% of atoms by $\pm 0.1\text{\AA}$.

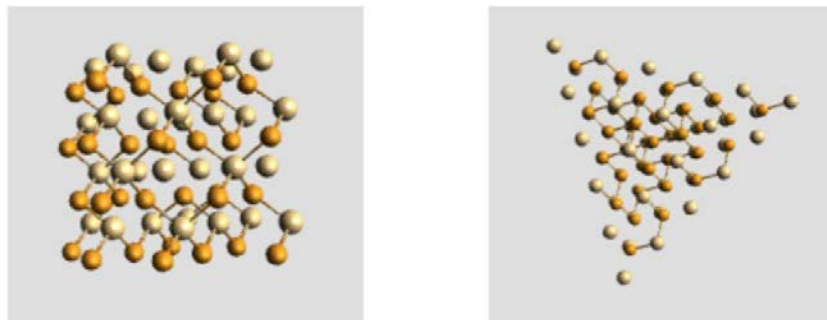


Figure 1: On the left, initial guess Zinc-blende bulk crystal CdSe structure; on the right, Owen-tetrahedral goal structure obtained from X-ray diffraction

Once a population of size N is generated, each candidate produces a mutated structure and a crossover structure, the details of these mechanisms will be described later in the methods section. Once both the crossover and mutation structure produced from the original candidate structure are generated, the fitness is evaluated. The fitness is evaluated based on the PDF data of the experimental versus the model data. An example of the comparison is shown below in Figure 2.

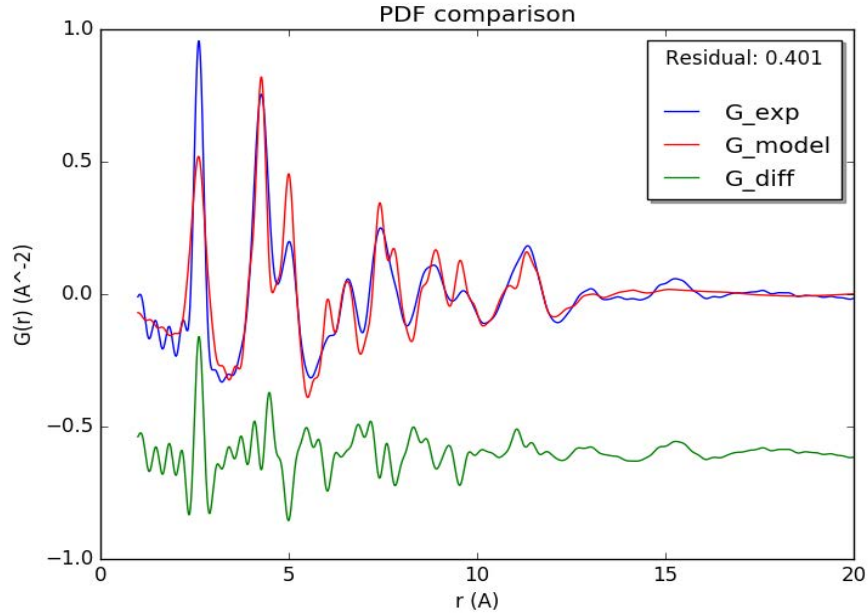


Figure 2: Atomic Pair Distribution function to display the fitness evaluation

The deviation between the experimental PDF data and the model data is represented by the "residual" value. The residual value is used as a way to represent the fitness of the structures moving onto the next generation. The residual value is given by Equation 1, as the squared difference between the probabilities, to give a global representation of how well the model fits the experimental.

$$R_w = \sqrt{\frac{\sum_{i=1}^N [G_{obs}(r_i) - G_{calc}(r_i; \vec{P})]^2}{\sum_{i=1}^N G_{obs}^2(r_i)}}$$

Equation 1: Residual Equation for Fitness Evaluation

Focusing back on the genetic algorithm, based on the residual values, whichever structure (mutated, crossover, original) has the lowest residual, and therefore the best fitness is chosen to move onto the next round of generations. This process of 1) mutated structure and crossover structure generation 2) fitness evaluation 3) redefine population repeats itself for a user-input number of generations or until the desired residual in the current population is reached.

Mutations

There are three types of mutations that can occur: addition, removal, and shifting. Mutations initially are set to only be addition movements, and the code tests to see if the addition of atoms helps to lower the residual. If the residual is not being lowered from adding atoms, the code switches to the removal of atoms. The addition of atoms occurs in places in the structure where the structure generated from the model should have more atoms in that location compared to the experimental PDF. Conversely, the removal of atoms occurs in places in which the model generated structure has a surplus of atoms in a location where the experimental data shows less atoms. Once the peaks of the experimental and model PDFs are no more than a distance of 0.5 on the y-axis away from each other, the adding/removal of atoms stops, and the shifting part of the mutations begin.

The shifting mutations are based on the concept of finding "deficits" and "surpluses". Given PDF data of both the experimental and the model structures, the code scans for the location $r(A)$ at which the two curves have the largest difference. This difference is then evaluated to be a deficit or a surplus. A deficit occurs when the experimental curve is above the model curve. This means that the model generated structure is lacking atoms at this distance of $r(A)$. A surplus occurs when the experimental curve is below the model, representing too many atoms at this distance in the model structure. Once the type of difference is defined, the code then scans nearby locations to $r(A)$ to see if any spots have the opposite difference. For example, if a deficit is detected, the code will search for a nearby surplus. From there, atoms are either shifted from the located surplus to the deficit location or atoms are shifted from the surplus location to the located deficit nearby. This methodology aims to have shifts in atoms fix the curve differences in two areas at once, rather than just adjusting one area on the curves. Appendix 1 shows a schematic of a shift mutation.

Crossovers

Crossovers are a random global shift of atoms. The mechanism for crossover shifting is quite simple. The code randomly selects 25% of atoms within the structure, then the code will randomly move each of those selected atoms by $\pm 0.05A$ in either the X, Y, or Z direction. The goal of a crossover is to provide to "mess up" the structure in a way that may have a lowering effect on the residual values.

III. Results and Discussion

Shown in Figure 1, the starting point for the code to test was the bulk Zinc-Blende CdSe structure. The code was typically run for a population of 10 candidates for between 1,000 to 2,000 generations. The runtime for this code was approximately 48 hours. In order to confirm the validity of the beneficial combination of crossovers and mutations within our code, we initially ran trials with just crossovers and just mutations then compared it to a run with both crossovers and mutations. In Figure 3 below, it can be

seen that the combination of crossovers and mutations has a greater effect on lowering the residual values of the structure candidates.

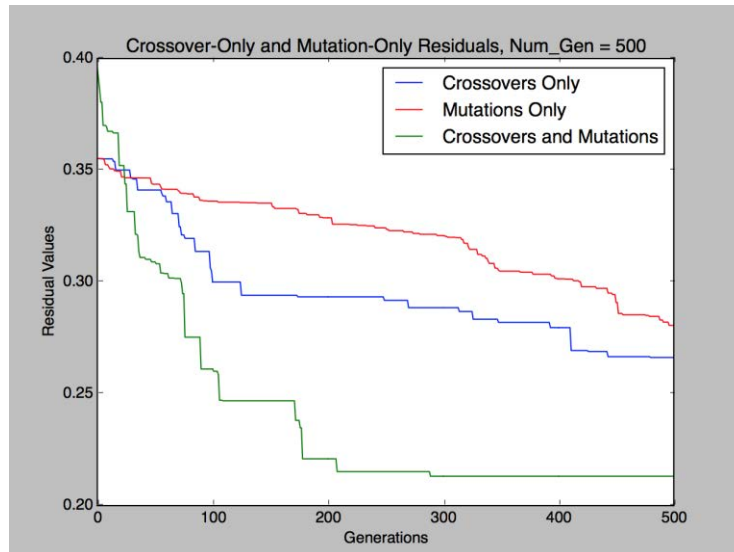


Figure 3: Residual value comparison of crossover and mutation effectiveness

When the code was run, it can be seen that some candidates in the population definitely do better than others, or in other words, some candidates are able to achieve a lower residual. This shows the benefit for running the model for a larger population, it gives the opportunity for more candidates to reach lower residuals. Shown below in Figure 4, is a run of a population of five candidates. The residuals all trend downward, which shows the effectiveness of the model. Each colored line represents the residuals of a candidate in the population over a certain number of generations.

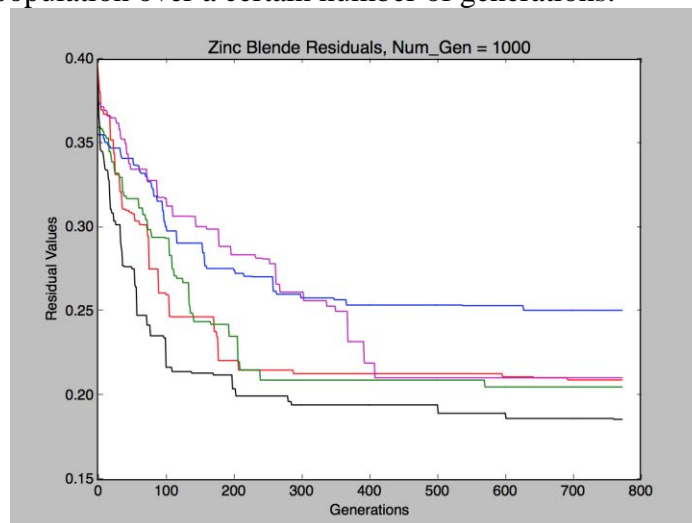


Figure 4: Overall representation of the residuals lowering over the course of 1000 generations for a population of 5

An overview of our best candidate over 2000 generations can be seen below in Figure 5. In examining the PDF of the experimental and model curve, it can be seen that the

difference between the two curves has decreased significantly from the initial PDF comparison shown in Figure 2. The residual value has decreased from 0.4 to 0.18, which is comparable to the literature values of "good" residuals seen at approximately 0.1-0.2. This indicates that our model for nanoparticle prediction is predicting structures with good residual values, and that over a series of generations, the curves of the experimental and the model become very close, meaning the structure the code is predicting is close to the true structure trying to be found.

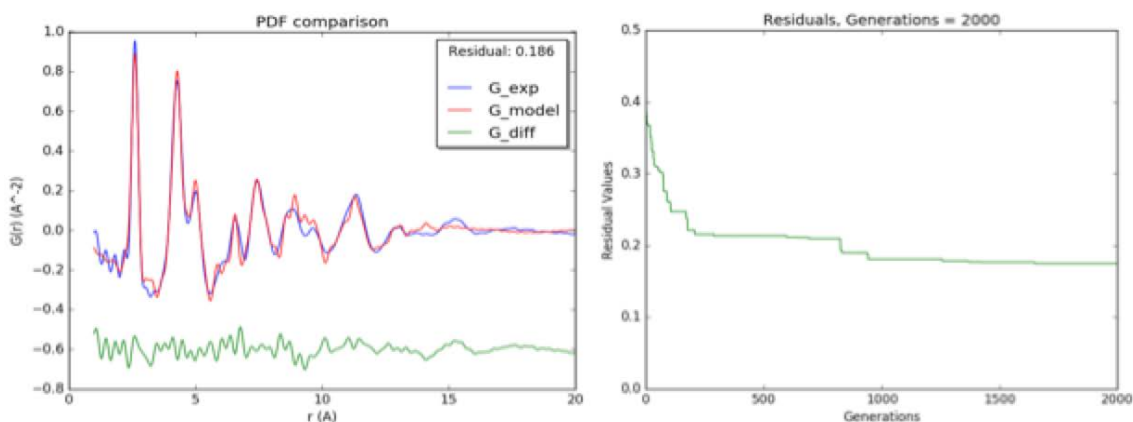


Figure 5: Lowered residual and closer PDF curves after 2000 trials for the CdSe structure

From this run described above, the structure that the code has predicted is accurate within a residual of 0.18. A comparison of the model's predicted structure and the Owen-tetrahedral goal structure mentioned in the methods section is shown in Figure 6. Although the predicted structure doesn't appear to be a perfect match for the goal structure, you can see from the rendering that the structure has moved away from the bulk cubic initial structure and is beginning to take the tetrahedral goal shape.



Figure 6: On the left, our computational model structure and on the right, the goal Owen tetrahedral structure

IV. Conclusion

The goal of this project was to create a computational model that would predict a nanoparticle structure with a residual of around 0.1 to 0.2. Our genetic algorithm proved to lower the residual by shifting the structure of a population of structure candidates. The genetic algorithm was a more intelligent search than a random method, which is crucial in this case because the search space is so large. The residuals achieved from our

computational model were around 0.18, which are comparable to literature values and fall within our range of residuals goal. The code is dynamic and can be used to predict the structure of any nanoparticle, not just a CdSe nanoparticle, which is what we used as our test case. With further refinement of the code, a lower residual could possibly be reached.

V. Acknowledgements

This work was supported by the Cornell Center for Materials Research with funding from the NSF Research Experience for Undergraduates program (DMR-1460428 and DMR-1120296).

[1] "*Quantum Dot Size and Color*".
<http://static1.squarespace.com/static/526856d7e4b05b8fbefaa9b6/t/52b12ad0e4b0d9c93d4c9460/1387342547474/qdsizes-spectrum.png>. Accessed 7 August 2016.

[2] Yang, X., Masadeh, A. S., McBride, J. R., Bozin, E. S., Rosenthal, S. J., & Billinge, S. J. L. "*Confirmation of disordered structure of ultrasmall CdSe nanoparticles from X-ray atomic pair distribution function analysis*" *Phys. Chem. Chem. Phys.*, 2013, 15, 8480.

[3] Proffen, Th., Billinge, S. J. L., & Egami, T. Louca, D. "*Structural analysis of complex materials using the atomic pair distribution function- a practical guide*". *Z. Kristallogr.* (2003) 132-143.

[4] Yu, M., Yankovick, A. B., Kaczmarowski, A., Morgan, D., & Voyles, P. M. "*Integrated Computational and Experimental Structure Refinement for Nanoparticles*". *ACS Nano* 2016, 10, 4031-4038.

[5] Beecher, A. N., Yang, X., Palmer, J. H., LaGrassa, A. L., Juhas, P., Billinge, S. J. L., & Owen, J. S. "*Atomic Structures and Gram Scale Synthesis of Three Tetrahedral Quantum Dots*". *J. Am. Chemical Society* 2014, 136, 10645-10653.

Effects of pH on the Gelation of High Concentration Collagen for Use in Bioprinting

Tylar Pruiksmas¹, Nicole Diamantides², Lawrence Bonassar^{2,3}

¹Department of Bioengineering, University of Utah, Salt Lake City, UT; ²Meinig School of Biomedical Engineering, Cornell University, Ithaca, NY, ³Sibley School of Mechanical Engineering, Cornell University, Ithaca, NY.

In recent years, 3D printing has emerged as an incredibly useful technology, and research is being done to bring this technology into the medical and biological space. Collagen is a biological material garnering much attention in this field due to its well known use in tissue engineering. Studies detailing collagen as a potential bioink have widely ruled it out as an option for its undesirable mechanical properties. For example, if gelation is too slow, the bioink will spread out after being printed. Most of these studies, however, have researched collagen at relatively low concentrations in the 0.5 mg/mL to 2.5 mg/mL range. To explore further potential of collagen as a bioink, we used rheology to analyze how a varying pH affected the moduli and gelation of 8 mg/mL collagen. Results showed that maximum storage modulus and maximum growth rate, both of which are vital to printability, occurred in the pH range of 7.8 to 9.1. This knowledge allows future research to focus in on the ideal pH range and invest in experimental printing and further mechanical testing to get one step closer to the realization of collagen as a bioink.

I. Introduction

Three-dimensional (3-D) printing has entered the forefront of scientific and technical innovation in recent years. 3-D printing is typically associated with melting down a plastic and extruding it through a fine tip where it can solidify once it exits and start to form some desired shape. As early as the late 1990s, extrusion based 3-D printing had already exhibited success in printing porous architectures [1]. Due to the success of this type of 3-D printing, researchers have been interested in using this technology in medical and biological applications. Bioprinting can be defined as “the spatial patterning of living cells and other biologics by stacking and assembling them using a computer-aided layer-by-layer deposition approach for fabrication of living tissue and organ analogs” for a variety of applications [2]. Based on this definition, it is clear that a variety of different materials can be considered for use as “bioinks.” Collagen is a particularly intriguing bioink not only because it is a natural polymer, but is also biocompatible, has cell binding sites, can encapsulate cells, and can be naturally degraded or remodeled [3].

When considering any material as a bioink, mechanical properties and gelation rate are of utmost importance. Collagen reacts differently to temperature than a plastic that is liquid at high temperatures and solid at lower temperatures. Because collagen is a natural polymer found in the body, its more solid state is actually at

body temperature, or 37° C , and is a liquid at lower temperatures. The bioink must solidify soon after being printed but not so soon that it does not print properly. The strength and elasticity of the final printed product are also important when considering the final engineered tissue that is desired. Collagen has been studied as a potential bioink, but has shown little promise thus far and is often written off. A variety of factors affect the mechanical properties and gelation of collagen, which include concentration, pH, temperature, source, and processing [4][5][6][7][8][9][10]. While studies have assessed the effects of these variables on collagen gelation, the concentrations used in such experiments have been in the relatively low range of 0.5 mg/mL to 2.5 mg/mL. At these concentrations, researchers have decided collagen may not be the ideal bioink. Other studies using similar concentrations, however, have demonstrated a relationship between pH and collagen gelation, even at low concentrations. Using turbidity, a measure of opacity, Li et al. (2009) demonstrated an evident relationship between pH and absorbance in 2.1 mg/mL collagen, as seen in Figure 1 [4]. Since collagen becomes more opaque as it gels, the slopes of the lines in the figure demonstrate the rate at which the collagen is gelling. As seen in the figure, there is a noticeable relationship between pH and the rate of collagen gelation.

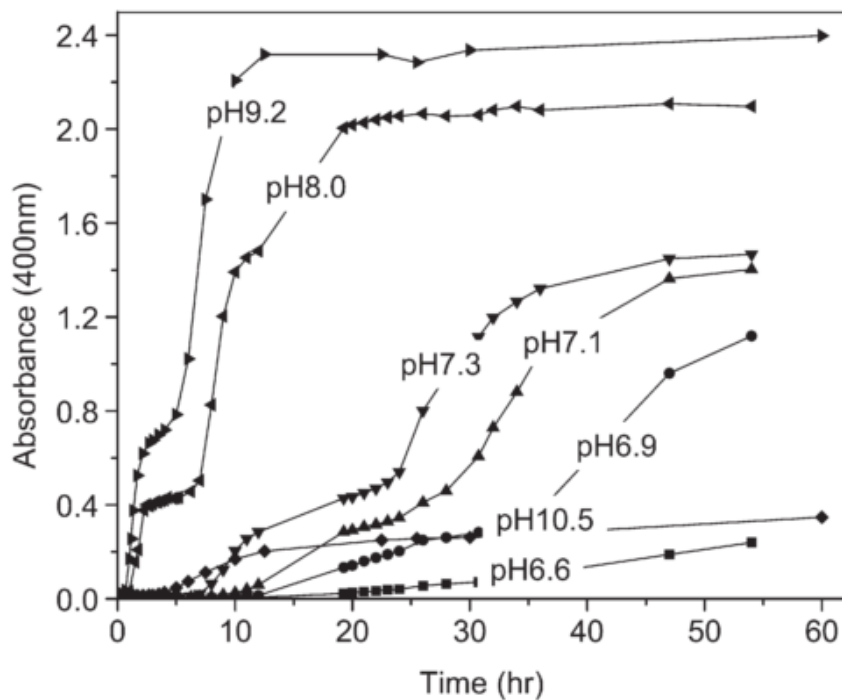


Figure 1: This graph shows turbidity results on collagen gels. The slope of each line is indicative of the rate at which the collagen solidified. Li et al (2009) [4].

Despite lack of success with low concentration collagen bioinks, there is still potential for collagen to be a realistic bioink. Since gelation has been shown to have dependence on pH in concentrations as low as 2.1 mg/mL, gelation may be even

more manipulable by varying pH in higher concentration collagen. For this study, high concentration collagen, at 8 mg/mL, was studied at varying pH using rheology to analyze the storage and loss moduli of the collagen gel as well as its rate of gelation. This information will provide knowledge of the ideal pH range to print in, as well as study the greater mechanical potential exhibited by higher concentration collagen gels.

II. Methods

Collagen Extraction

Type I collagen is extracted from rat tail tendons. Prior to extraction, the rat tails were kept frozen and were thawed in ethanol in preparation for use. Once thawed, the tail was cut at the nearest vertebrae to each end of the tail. An incision was then made down the length of the tail. Using this incision, the tail was skinned and the skin was discarded. Starting from the side proximal to the body, each of the four tendon bundles was pulled away from the vertebrae and towards the distal end of the tail until the entire tendon had been removed. The extracted tendons were stored in ethanol until all tendons had been removed. The tendons in ethanol were then thoroughly dried and weighed. Once the mass was known, the dried tendons were placed in a solution of 0.1% acetic acid (HAc) at 150 mL per milligram of tendons. This solution was then refrigerated for at least 48 hours.

Collagen Preparation

After the tendons had been in the 0.1% HAc solution for 48 hours, the aqueous component of the mixture was removed and spun down using a centrifuge at 9000 rpm for 90 minutes. Once the solid portion of the mixture had been spun down, the supernatant was removed and isolated. This aqueous solution was then frozen at -80° C for at least 24 hours. Once frozen for 24 hours, the collagen solution was then lyophilized for 4 to 5 days before being reconstituted in 0.1% HAc at a concentration of 15 mg/mL.

Surface Activation

To ensure covalent bonding between the collagen and the rheometer to prevent wall slip, surface-activated glass cover slides were attached to the rheometer plates. Glass cover slides 25 mm in diameter were placed on a piece of double-sided tape attached to a piece of Parafilm. The glass cover slides were first treated with 1% polyethylenimine for 10 minutes and rinsed once with distilled water. They were then treated with 0.1% glutaraldehyde for 30 minutes and then rinsed three times with distilled water. They were then allowed to dry before use in rheology.

Working Solution

8 mg/mL collagen solutions were prepared by diluting 15 mg/mL collagen with a working solution to a final volume of 5 mL. For the collagen, 2.67 mL of collagen was put in a syringe and kept on ice. For the working solution, the total was always 2.33 mL. Each time, 0.50 mL of 10X phosphate buffered saline (PBS) were

used, but the amount of 1 M NaOH and 1X PBS used changed depending on the desired pH of the final sample. The volume of 1M NaOH used varied from 20 μ L to 75 μ L. To reach a total volume of 5 mL, the corresponding volume of 1X PBS was added. This working solution was also put in a syringe and kept on ice until needed for rheology. When preparing for rheology, these two solutions were mixed using a three-way stop-cock 60 times before loading the sample onto the rheometer.

Rheology

All rheology was done on the Anton Parr 501 rheometer in the Center for Nanomaterials Engineering and Technology facilities at Cornell University. The rheometer is set up using 25 mm parallel plates and the previously prepared glass cover slips were attached to each plate using the double-sided tape. Once the collagen sample had been loaded and the plates were at the test gap of 1.0 mm, mineral oil was added to the perimeter of the parallel plate to prevent sample dehydration. The rheometer tests were performed in oscillatory mode at 0.1 Hz and 0.5% strain. The starting temperature was 4° C. After 5 minutes, the temperature controlled plate raised the temperature to 37° C, at which the collagen gel remained for an additional hour of testing.

pH Measurement

After rheology the remaining sample was kept on ice and the pH of the sample was measured using the pH meter in the Bonassar lab in Weill Hall of Cornell University. The pH meter was first cleaned with deionized water and then calibrated using 4.00, 7.00, and 10.00 pH solutions. Once calibrated, the pH meter was used to measure the pH of the collagen sample three times, and these values were recorded.

III. Results

From rheology, a variety of data is available, but our analysis focused on storage modulus, loss modulus, complex viscosity, phase angle, growth rate, and crossover time. In Figure 2, a typical storage and loss modulus curve is shown to explain how this data appears. Storage modulus is a measure of elastic response and loss modulus is a measure of viscous behavior. The crossover point shows the point in time at which the storage modulus overtakes the loss modulus. The maximum growth rate along the curve shows how quickly the collagen gels once the temperature has been increased to 37° C from 4° C.

Rheology was run 16 times with a variety of different pHs. The working solutions had varying volumes of 1 M NaOH and 1X PBS to change the pH. When measuring pH after rheology, these volumes corresponded to collagen in a pH range of 6.21 to 9.59.

When considering valuable data for the possibility of printing, storage modulus is extremely important, as it measures elastic response and can correspond

to gelled collagen's ability to hold its shape. As seen in Figure 3, the maximum storage modulus reached by a sample is dependent on pH. The highest storage modulus found was 1898.8 Pa for the pH 7.8 collagen. The lowest storage modulus found was 475.5 Pa for the pH 6.48 collagen. Maximum storage modulus was generally highest in the pH range of 7.8 to 9.1 range.

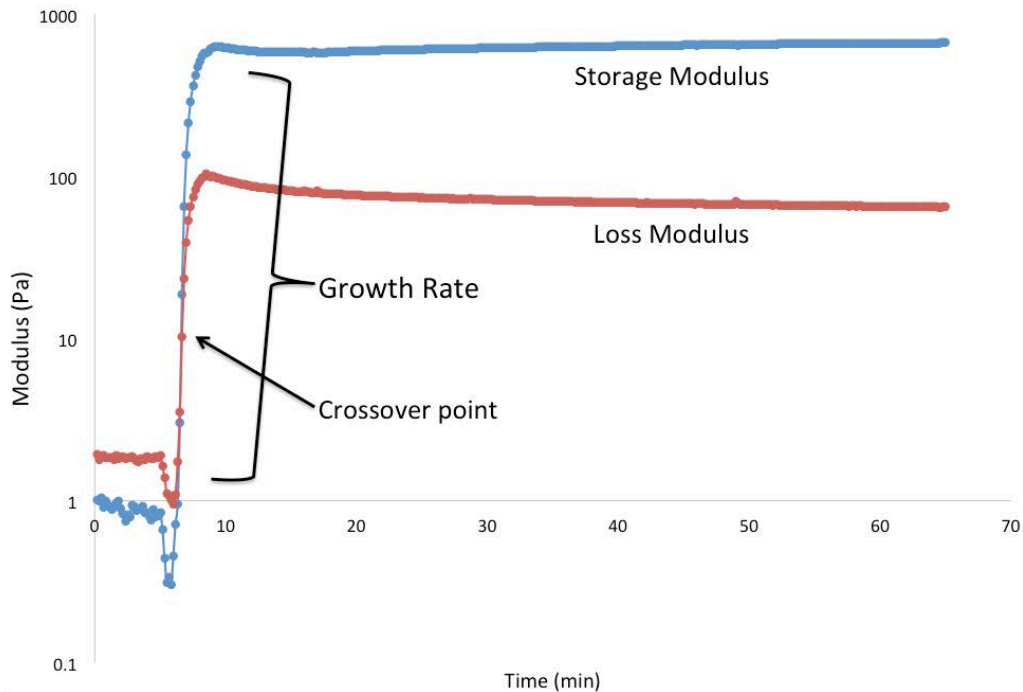


Figure 2: A typical storage and loss modulus curve, with labels of each modulus, the growth rate, and the crossover point.

The pH of a collagen gel also affects its growth rate. Along with storage modulus, growth rate is the other vital piece of data when making considerations for printing. If the growth rate is too fast, the collagen will gel before it can be printed, but if the growth rate is too slow, the gel will spread once it has been printed. As seen in Figure 4, the distribution of growth rate data closely resembles the data seen in Figure 3 representing maximum storage modulus. Just like storage modulus, the maximum growth rate was found at a pH of 7.8, and the minimum growth rate was at a pH of 6.48. Unlike storage modulus though, growth rate tapered off sooner, and started to drop off at pH above 8.47.

While storage modulus and growth rate demonstrate a clear dependency on pH, crossover time does not. Throughout testing, crossover time was extremely consistent and nearly always occurred between 75 and 100 seconds after the temperature was increased to 37° C. The small variations in crossover time show no relationship or dependency to pH, so it can be concluded that pH is a non-factor when studying crossover time in collagen gel.

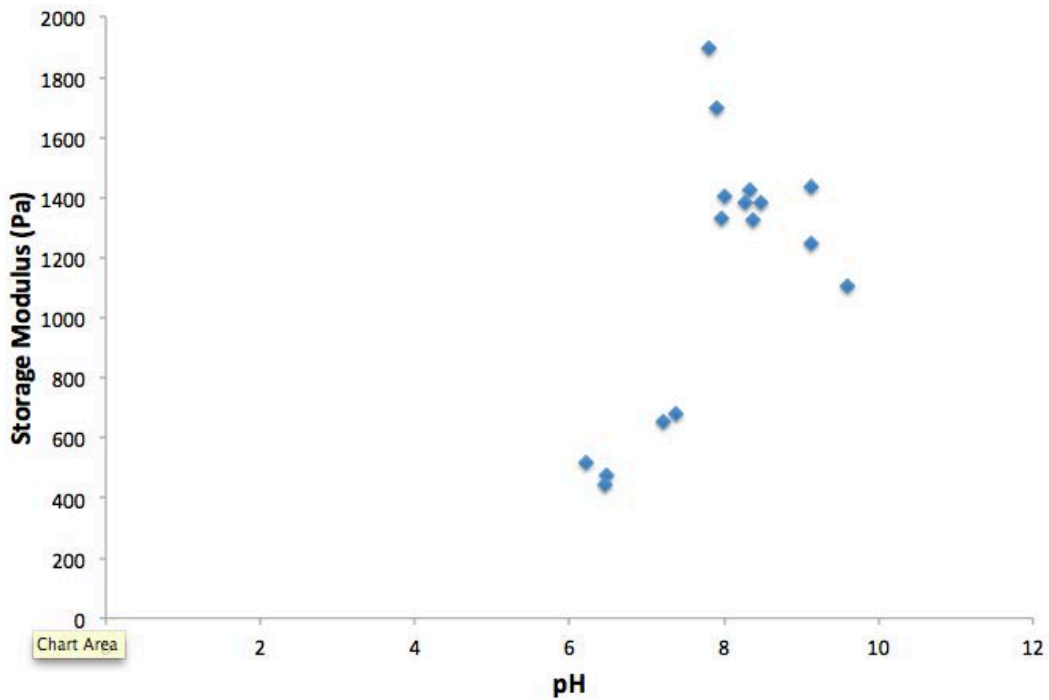


Figure 3: A graph demonstrating how pH affects the maximum storage modulus reached by a collagen gel during testing.

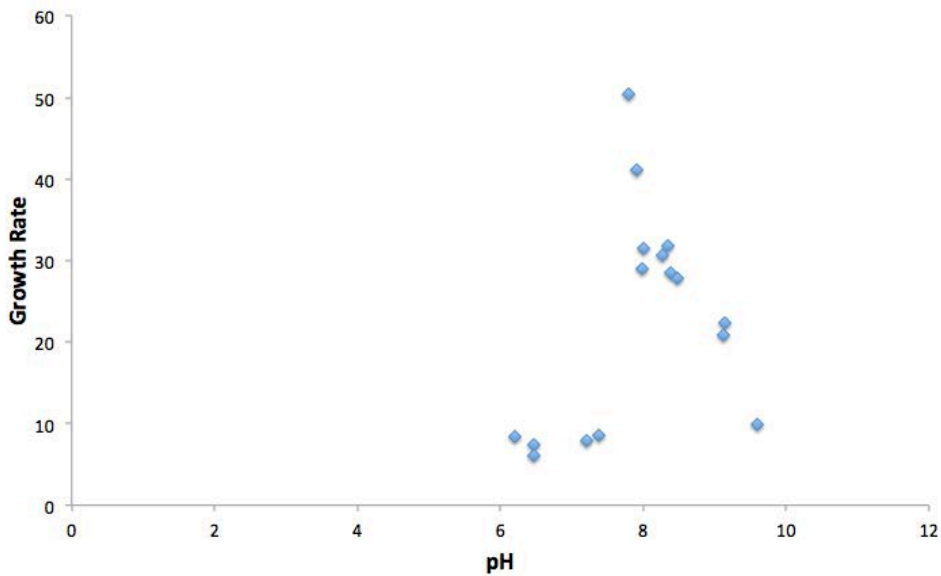


Figure 4: A graph demonstrating how pH affects the growth rate experienced by a collagen gel during testing.

The data shown in Figure 3 and Figure 4 come from collagen samples from a variety of batches, so batch variability must be considered. After the initial trials were complete, rheology tests were performed across the pH spectrum using only one collagen batch to control variability. As seen in Figure 5 and Figure 6, these tests

were consistent with the original trials, and showed maximum storage modulus and growth rate near pH 8, similarly to the original tests.

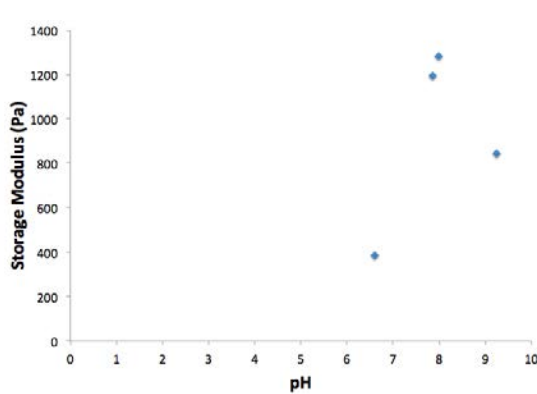


Figure 5: Maximum storage modulus for collagen gels from the same batch.

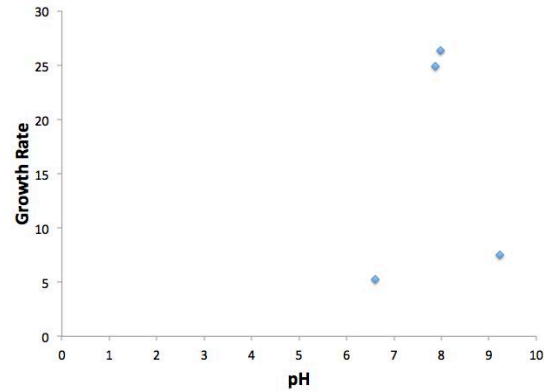


Figure 6: Maximum growth rate for collagen gels from the same batch.

While no numerical data was collected on tensile strength, noticeable tensile properties were observable amongst the collagen gels of varying pH. Qualitatively, the strongest and seemingly most elastic gels belonged to the collagen in the 9.1 to 9.6 pH range. These strength observations are not perfectly consistent, however, with the maximum storage modulus values in the 7.8 to 9.1 range.

IV. Discussion and Conclusion

Storage modulus and growth rate of a higher concentration collagen gel are indeed dependent on pH. When studied across a pH range from 6.21 to 9.59, both maximum storage modulus and maximum growth rate fell into the pH range of 7.8 to 9.1 and showed similar curves over the entirety of the pH range. When looking back at the data from the Li et al. (2009) study, these values make sense. The highest absorbances, which are analogous to storage modulus, and the highest slopes, which are analogous to growth rate, were at pH 9.2 and 8.0 [4]. Even at a comparatively lower concentration of 2.1 mg/mL, the data from rheology performed on 8.0 mg/mL collagen supports the conclusion that strong mechanical properties and fast gelation rates occur at pH in the high 7 to low 9 range.

When assessing the qualitative observations that the “strongest” gels were in the pH range of 9.1 to 9.6, it is important to note that this is not the same range that holds the maximum storage modulus values from the study. This may be indicative that storage modulus, while an important measurement of elastic response, may not be the most accurate piece of data for evaluating the mechanical strength of collagen.

Moving forward with this knowledge, further mechanical testing, such as compression testing, may be useful in differentiating the respective strengths of collagen at the high storage modulus pH values and the high “strength” pH values.

Ultimately, two of the most important values when considering potential bioinks, storage modulus and growth rate, were shown to be dependent on pH in higher concentration collagen. Using this information and the pH range in which these two values are high, future collagen bioprinting research can be more focused on a specific pH range. This increased focus opens the door to experimentation with the other factors that affect gelation, such as temperature, source, and processing.

With a newly focused pH range, more time can be invested testing the actual 3-D printing abilities of these collagen gels, and further progress can be made towards the eventual goal of successful 3-D bioprinting.

V. Acknowledgments

This work was supported by the Cornell Center for Materials Research with funding from the NSF Research Experience for Undergraduates program (DMR-1460428 and DMR-11120296). I would like to thank the Center for Nanomaterials Engineering and Technology for use of their facilities. I would also like to thank Nicole Diamantides and Professor Larry Bonassar for their continuous help and support.

VI. References

- [1] H. Lipson, M. Kurman, *Fabricated: the New World of 3D Printing*, Wiley, 2013
- [2] I. Ozbolat, M. Hospodiuk, Current advances and future perspectives in extrusion-based bioprinting. *Biomaterials*, 76(2016), pp.321-343.
- [3] Murphy SV, Skardal A, Atala A. 2013. Evaluation of hydrogels for bio-printing applications. *J Biomed Mater Res Part A* 2013;101A:272–284.
- [4] Y. Li, A. Asadi, E.P. Douglas, *et al.* pH effects on collagen fibrillogenesis in viro: Electrostatic interactions and phosphate binding. *Mater. Sci. Eng. C.*, 29(2009), pp. 1643-1649.
- [5] J. Harris, A. Soliakov, R. Lewis. 2013. In vitro fibrillogenesis of collagen type I in varying ionic and pH conditions. *Micron*. 2013.
- [6] J. Snowden, D. Swann. 1979. The formation and thermal stability of in vitro assembled fibrils from acid-soluble and pepsin-treated collagens. *BBA-Protein Structure*. 1979.
- [7] S. Wilson, M. Guilbert, et al. 2014. A microscopic and macroscopic study of aging collagen on its molecular structure, mechanical properties, and cellular response. *FASEB journal*. 2014.
- [8] D. Zeugolis, R. Paul, G. Attenburrow. 2008. Factors influencing the properties of reconstituted collagen fibers prior to self-assembly: Animal species and collagen extraction method. *Journal of Biomedical Materials Research*. 2008.
- [9] C. Raub, V. Suresh, et al. Noninvasive assessment of collagen gel microstructure and mechanics using multiphoton microscopy. *Biophysical journal*. 2007.
- [10] M. Achilli, D. Mantovani. 2010. Tailoring mechanical properties of collagen-based scaffolds for vascular tissue engineering: The effects of pH, temperature and ionic strength on gelation. *Polymers*. 2010.

Lysine Palmitoylation of HRas and RalB Proteins

Kelly Rosch, Nicole Spiegelman & Dr. Hening Lin
Cornell University Department of Chemistry & Chemical Biology

Introduction

Ras and Ras-like proteins are small GTPases, meaning they are involved in the process of converting guanosine triphosphate (GTP) into guanosine diphosphate (GDP) [1]. These small GTPases are typically involved in cell signaling and cell division, but when the genes that encode them become mutated, they can cause uncontrolled cell division, resulting in cancer [2]. The genes that encode Ras proteins are the most common oncogenes in human cancer, and mutations in these genes cause up to 95% of pancreatic cancers [3].

Proteins can have post-translational modifications, meaning that they can be modified by small chemical groups after they have been translated. These chemical modifications can play a role in determining the localization and function of the proteins. For example, previous research has indicated that cysteine palmitoylation anchors a protein to the cell membrane, and removal of cysteine palmitoylation removes this anchor, releasing the protein into the cytosol [4]. Studying these chemical modifications on Ras and Ras-like proteins may offer clues to the roles that they play in human cancers.

Previous research has shown that HRas, a protein in the Ras family, and RalB, a protein in the Ras-like family, typically undergo lipid modifications such as cysteine palmitoylation and cysteine prenylation [5]. During cysteine palmitoylation, palmitic acid is added to a cysteine amino acid in the protein forming a thioester bond. Additionally cysteines can also undergo prenylation, where the cysteine residue can be modified by a farnesyl or a geranyl-geranyl group.

The Lin group recently found a third type of lipid modification that may occur on the Ras related GTPases: lysine palmitoylation. Lysine palmitoylation is the covalent attachment of palmitic acid to a lysine residue. Here we wanted to determine if the two small GTPases RalB and HRas have lysine fatty acylation.

Methods

Quick Change Mutagenesis Polymerase Chain Reaction (PCR)

RalB and HRas mutants were prepared using quick-change mutagenesis PCR. The following solutions were prepared in separate PCR tubes for each sample: 32 μL water, 0.5 μL forward primer, 0.5 μL reverse primer, 2 μL deoxynucleotide triphosphates (dNTP), 2 μL dimethyl sulfoxide (DMSO), 2 μL cDNA template (200ng/ μL), and 10 μL 5X HF Buffer. Then 1 μL of Phusion High Fidelity DNA Polymerase was added to each PCR tube. The tubes were placed in a thermocycler and the appropriate times and temperatures were selected for the PCR reaction to occur based on standard protocols. All constructs were verified by sequencing.

Transfection, Alkyne-14 Treatment, Cell Lysis, and Bradford Assay

Cells were transfected at 40-60% confluency. Cell media was replaced with 10 mL of fresh media supplemented with 10% Fetal Bovine Serum (FBS). Fugene 6 transfection reagent was combined with the plasmid in a 3:1 ratio following the manufacturer's protocol. The Fugene 6 and plasmid mixture was added to the corresponding plate of cells, and the cells were allowed to grow for 16 hours. After 16 hours, the cell media was

changed to media with 10% FBS supplemented with 50 μ M Alkyne-14. After 6 hours, the cells were collected and washed twice with phosphate buffered saline (PBS). The cells were then lysed with 400 μ L of 1% NP40 lysis buffer supplemented with Protease Inhibitor Cocktail (PIC). The protein concentration of the lysate was measured using a Bradford assay.

Immunoprecipitation, Click Chemistry, and Fluorescence Gel

After protein normalization, equal amounts of overexpressed proteins were pulled out from the total cell lysate by Flag Immunoprecipitation. The lysate volume was brought to 1 mL with 0.2% NP40 buffer. Then 20 μ L of prewashed Flag beads were added to each sample. The samples were placed on the rocker at 4°C for two hours. The samples were then washed three times with 1 mL 0.2% NP40 buffer. After the third wash, the beads were dried and resuspended in 20 μ L 0.2% NP40 buffer. To allow for visualization of lysine palmitoylation, a fluorophore was attached to the Alkyne-14 probe using click chemistry. For this reaction, 1 μ L of each reagent (1 μ M Bodipy azide, 10 μ M Tris[(1-benzyl-1H-1,2,3-triazol-4-yl)methyl]amine (TBTA), 40 μ M copper sulfate, and 40 μ M Tris(2-carboxyethyl)phosphine (TCEP)) was added to each sample. After 30 minutes, the click reaction was quenched by adding 10 μ L 6x protein loading dye. The samples were boiled at 95°C for 7 minutes. To remove cysteine palmitoylation, half of the sample was treated with hydroxylamine (330 μ M final concentration) at 95°C for 7 additional minutes. The samples were resolved by protein gel and fluorescence was visualized on a Typhoon scanner.

Results

To determine if HRas or RalB had lysine palmitoylation, the fluorescence signal of both the wild type and lysine deficient proteins was compared. For HRas a 3 lysine-to-arginine mutant and for RalB an 8 lysine-to-arginine mutant was generated. (Figure 1 and 2). Arginine was chosen because it has the same charge and size as lysine but cannot be palmitoylated. Additional mutants were generated to help identify which lysine residues of these proteins are fatty acylated. The mutants that were cloned are shown in Figure 1.

Figure 1. Diagrams indicating which lysine residues (abbreviated “K”) were mutated to arginine in each mutant group on the RalB C terminal (top) and the HRas C terminal (bottom).

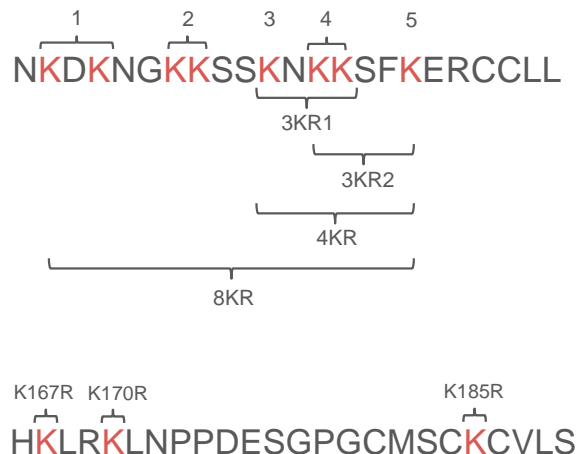


Figure 2. Fluorescence gel comparing HRas wild type (WT) to an HRas 3KR mutant.

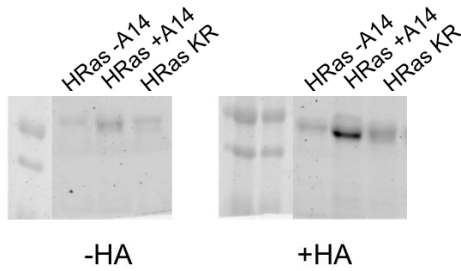
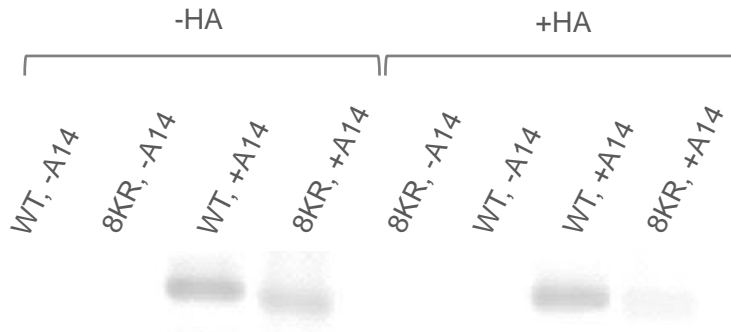


Figure 3. Fluorescence gel comparing WT RalB to 8KR RalB.



Past research suggests that RalB undergoes cysteine palmitoylation; this is supported by the fact that the fluorescent signal decreases after hydroxylamine treatment. These gels indicate that RalB has lysine palmitoylation because RalB 8KR has a strong signal in the blue gel (indicating high protein loading) but a weak signal in the fluorescence gel compared to the wild type RalB. It appears as if the last few lysine residues in RalB may have lysine palmitoylation. While the protein loading is lower (blue gel in Figure 5), the fluorescence signal is also significantly lower for RalB M3 and RalB M5.

Figure 4. Fluorescence gel (left) and blue gel (right) comparing RalB WT to KR mutant groups after hydroxylamine treatment. The blue gel indicates total protein loaded, and the fluorescence gel indicates presence of lysine palmitoylation.

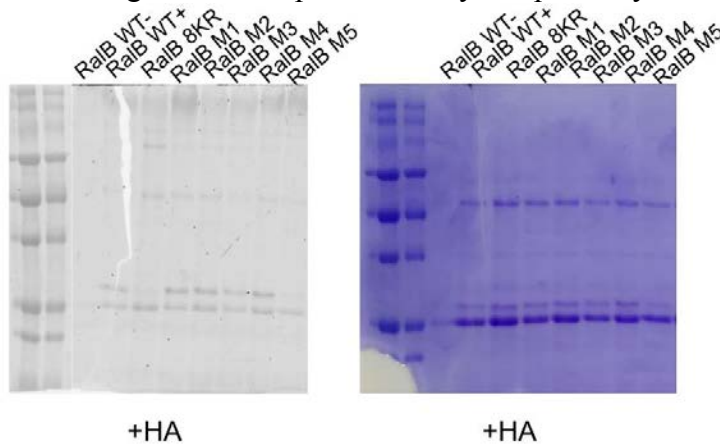
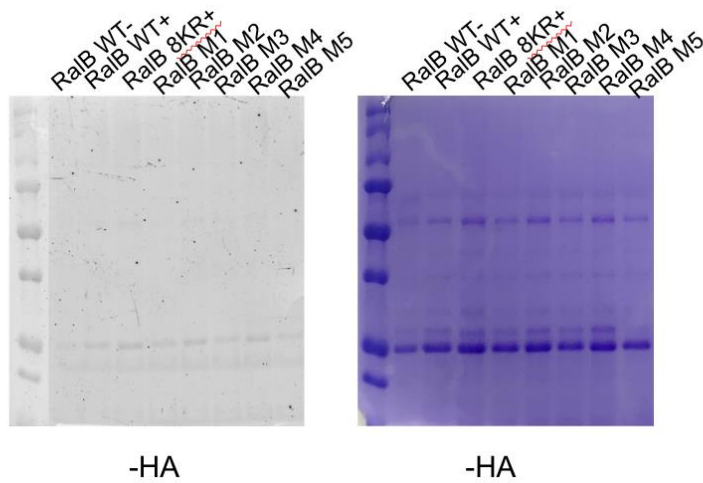


Figure 5. Fluorescence gel (left) and blue gel (right) comparing RalB WT to KR mutant groups before hydroxylamine treatment. The blue gel indicates total protein loaded, and the fluorescence gel indicates presence of lysine palmitoylation.



Discussion

Results support the Lin lab's previous findings that lysine palmitoylation is a modification found on various small GTPases. Here it is shown that both HRas and RalB appear to have lysine palmitoylation. Future research should continue to study which lysine residues in RalB and HRas are palmitoylated using the constructs that were cloned in this experiment. While past research has indicated that cysteine palmitoylation anchors the protein to the cell membrane, lysine palmitoylation has not been studied in depth. Future research will investigate the function of lysine palmitoylation on RalB and HRas, as well as determine the mechanism for adding and removing this modification. Understanding the role of lysine palmitoylation on HRas and RalB may help elucidate the role that these proteins play in metabolism or cancer.

References

- [1] Gentry LR, Martin TD, Reiner DJ, Der CJ. Ral small GTPase signaling and oncogenesis: more than just 15 minutes of fame. *Biochimica et biophysica acta*. 2014;1843(12):2976-2988. doi:10.1016/j.bbamcr.2014.09.004.
- [2] Fernández-Medarde, A.; Santos, E. Ras in Cancer and Developmental Diseases <http://www.ncbi.nlm.nih.gov/pmc/articles/pmc3128640/> (accessed Aug 9, 2016).
- [3] The RAS Problem <http://www.cancer.gov/research/key-initiatives/ras/the-problem> (accessed Aug 9, 2016).
- [4] Overview of Post-Translational Modifications (PTMs) <https://www.thermofisher.com/us/en/home/life-science/protein-biology/protein-biology-learning-center/protein-biology-resource-library/pierce-protein-methods/overview-post-translational-modification.html> (accessed Aug 9, 2016).
- [5] Laude, Alex J., and Ian A. Prior. "Palmitoylation and localisation of RAS isoforms are modulated by the hypervariable linker domain." *Journal of cell science* 121.4 (2008): 421-427.

Imaging Extracellular Vesicles (EV's) using Transmission Electron Microscopy (TEM)

Julio Vazquez¹, Jack Hartman², Fredrik Thege², Brian Kirby⁴, John Grazul⁴

CCMR¹, Bioengineering Department², Biomedical Engineering Department³, Engineering Department⁴

Abstract

A vesicle is a small structure within a cell that transports material such as proteins and nucleic acids. Recently it was discovered that cells shed vesicles to different bodily fluids as a form of intercellular communication^{1,2,3}. These are called Extracellular Vesicles (EV's). Research has shown that EV's from cancer cells are likely to play an important role in metastasis^{2,7}. The focus of this research is to image EV's using Transmission Electron Microscopy (TEM)^{6,7}. We experimented with three different methods to prepare samples which consists of a "Whole Mounted"⁴ procedure, implementing the use of Methylcellulose (MC) to our "Whole Mounted"⁴ procedure and lastly we experimented with Immunogold Labeling (IGL) to track the CD63 protein membrane that EV's have proven to contain³. We effectively gathered representative images using the "Whole Mounted" procedure where EV's can be seen based on their round-cup shaped morphology^{1,2,3,4}. With the use of MC we effectively generated better background and the possibility to image inside the holes of "Holey Grids". The IGL process stills need to be refined since we didn't achieved specific binding. Based on the images gathered it is possible to effectively measure size and concentration of EV's using image processing software's.

Introduction

EV's are vesicles that cells shed as a form of intracellular communication^{1,2}. They contain cytosolic proteins, lipids, and RNA [1] that lead to the exchange of genetic information and reprogramming of the recipient cell^{2,3,5}. EV's can be divided into three sub-groups which are categorized by where they originated and also differ in sizes^{1,6,7}. These are exosomes, microvesicles and apoptotic bodies^{1,2,3,4}. Exosomes generate inside the cell and then are shed out^{1,2}, microvesicles form directly on the cell membrane and then are shed out^{1,6,7,8}. Apoptotic bodies generate from dying cells¹. Out of the three sub-populations, we are interested in exosomes and microvesicle since they are specifically packed with proteins that resemble ones from inside the cell they originated¹. Apoptotic bodies just contain a random sample of the dead cell they originated from¹.

Research has shown that cancer cells release an excessive amount of EV's. Increasing evidence suggest that they may influence tumor imitation, growth, progression metastasis and drug resistance^{3,5}. Based on this, they have become very attractive because they can lead to biological research and potentially serve as biomarkers for cancer diagnosis and serve as a drug delivery vehicle that specifically targets cancer cells^{3,5}. This is very attractive since we can essentially directly treat the afflicted cells instead of killing all cells in the tumor area as it is the case with chemotherapy^{3,5}. Since EV's differ in sizes^{1,2}, it is in our interest to accurately and quickly image EV's to be able to measure their size and concentration to further enable biological research^{1,2}.

Since EV's sizes ranges from 40-100 nm (Exosomes) and 100-500 nm (microvesicles)^{1,2,8}, we had to use TEM instead of normal Light Microscope due to the resolving power of TEM. Since electrons have a shorter wavelength, TEM lets us image at the nano scale. The way TEM works is by shooting an electron beam under a vacuum that passes through our sample and generates an image in a fluorescence screen^{7,8}. Since the samples are going under a vacuum, they must be dead. Because of this, the samples

must be prepared in specific way prior to imaging. The general sample preparing process consist of fixing, dehydration, embedding, sectioning and staining⁴.

Fixing is done to preserve the dead sample closest to its living state. Dehydration is done to remove the excess of liquid in the sample so it doesn't interrupt when the electron beam hits the sample.

Embedding is basically adding a plastic resin to the sample so it can be then sectioned. Sectioning is simply cutting the sample in very thin slices. This is done to allow the electron beam to pass through our sample. Finally staining is coating the sample with heavy metals to add electron density to our sample and generate contrast when imaging.

To prepare our samples for imaging, we first used a technique called "Whole Mounted" procedure⁴. This process is called this way because it doesn't involve embedding nor sectioning. Since EV's are very small compared to cells, it is impractical and very difficult to apply these steps⁴. Our goal was to show that we had vesicles in our sample. We first based our methodology from Clothilde They procedure and then optimize it based on our results.

For our second sample prepped technique we applied the use of methylcellulose (MC) to the "Whole Mounted" procedure⁴. MC is a white powder in its original form that when mixed with water forms a viscous, glue like solution. The purpose was to generate better contrast and background.

Our third sample preparing way consisted of Immunogold Labeling (IGL)^{4,9}. IGL is a process where antibodies are used to target specific proteins (in our case CD63³) with gold nanoparticles. The purpose of this experiment was to further prove we have vesicles by targeting the CD63 membrane protein that EV's contain³.

Methodology

Whole Mounted Procedure (Based from Clothilde They Procedure)⁴

First the samples where fixed with 2% Paraformaldehyde (PFA) overnight. Then add 10uL of sample on clean Parafilm. Deposit the EM Formvar-carbon coated EM "holey grids" and let the grids adsorb the sample for 20min. Remove excess fluid by gently placing the membrane side of the grid on filter paper and quickly remove it, you should never let go of the sample while doing this step. Add 100uL of PBS on Parafilm and transfer the grids (membrane side down) to the drops of PBS for 2min for a wash. Remove excess fluid as explained before. Add 50uL of 1% Glutaraldehyde (GA) on clean Parafilm and transfer grids membrane side down for 5min for post-fixing. Remove excess fluid as explained before. Transfer grids to a 100uL drop of distilled water for a wash for 2min, repeat 7 times for a total of 8 washes, in between each wash remove excess fluid as explained before. Transfer grids to a drop of 2% Uranyl Acetate (UA) membrane side down for 10min for staining, removed excess fluid as explained before. Image on TEM at 80kV.

Later this process was optimized by fixing for 20min instead of Overnight. The PBS wash was removed. The post-fixing with GA was removed. The x8 washes with distilled water for 2 min where cut down to x4 washes where instead of letting the grid stand on the droplet, we hold it with tweezers and gently submerged the membrane side of the grid for 3 seconds while moving it around in the droplet without never letting it go. The staining time with 2% UA was cut down to 10 seconds.

Optimized “Whole Mounted” procedure⁴

First the samples were fixed with 2% Paraformaldehyde (PFA) for 20 minutes. Then add 10uL of sample on clean Parafilm. Deposit the EM Formvar-carbon coated EM “holey grids” and let the grids adsorb the sample for 20min. Remove excess fluid by gently placing the membrane side of the grid on filter paper and quickly remove it, you should never let go of the sample while doing this step. Wash grids in 100uL drop of distilled water without releasing the grids as explained before for 3 seconds, repeat 3 times for a total of 4 washes, in between each wash remove excess fluid as explained before. Gently submerged grids to a drop of 2% Uranyl Acetate (UA) membrane side down for 10 seconds for staining without letting go of the grids as explained before, removed excess fluid as explained before. Image on TEM at 80kV.

Whole Mounted procedure with Methylcellulose (MC)⁴

First the samples were fixed with 2% Paraformaldehyde (PFA) overnight. Then add 10uL of sample on clean Parafilm. Deposit the EM Formvar-carbon coated EM “holey grids” and let the grids adsorb the sample for 20min. Remove excess fluid by gently placing the membrane side of the grid on filter paper and quickly remove it, you should never let go of the sample while doing this step. Add 100uL of PBS on Parafilm and transfer the grids (membrane side down) to the drops of PBS for 2min for a wash. Remove excess fluid as explained before. Add 50uL of 1% Glutaraldehyde (GA) on clean Parafilm and transfer grids membrane side down for 5min for post-fixing. Remove excess fluid as explained before. Transfer grids to a 100uL drop of distilled water for a wash for 2min, repeat 7 times for a total of 8 washes, in between each wash remove excess fluid as explained before. Transfer grids to a drop of 2% Uranyl Acetate (UA) membrane side down for 10min for staining, removed excess fluid as explained before. Transfer the grids to 50uL drop of 2% methylcellulose/2% Uranyl Acetate for 10 min on ice. Remove excess fluid as explained before. Let air dry for 10 min by putting the grid on filter paper membrane side up. Image on TEM at 80kV.

This process was optimized the same way the “Whole Mounted” procedure was optimized. Also we separated the combination of 2%MC/2%UA to just 2%MC.

Optimized Whole Mounted procedure with Methylcellulose (MC)

First the samples were fixed with 2% Paraformaldehyde (PFA) overnight. Then add 10uL of sample on clean Parafilm. Deposit the EM Formvar-carbon coated EM “holey grids” and let the grids adsorb the sample for 20min. Remove excess fluid by gently placing the membrane side of the grid on filter paper and quickly remove it, you should never let go of the sample while doing this step. Add 100uL of PBS on Parafilm and transfer the grids (membrane side down) to the drops of PBS for 2min for a wash. Remove excess fluid as explained before. Add 50uL of 1% Glutaraldehyde (GA) on clean Parafilm and transfer grids membrane side down for 5min for post-fixing. Remove excess fluid as explained before. Transfer grids to a 100uL drop of distilled water for a wash for 2min, repeat 7 times for a total of 8 washes, in between each wash remove excess fluid as explained before. Transfer grids to a drop of 2% Uranyl Acetate (UA) membrane side down for 10min for staining, removed excess fluid as explained before. Transfer the grids to 50uL drop of 2% methylcellulose for 10 min on ice. Remove excess fluid as

explained before. Let air dry for 10 min by putting the grid on filter paper membrane side up. Image on TEM at 80kV.

Immunogold Labeling^{4,9}

Fix samples with 2% PFA overnight. Then add 10uL of sample on clean Parafilm. Deposit the EM Formvar-carbon coated EM "holey grids" and let the grids adsorb the sample for 20min. Remove excess fluid by gently placing the membrane side of the grid on filter paper and quickly remove it, you should never let go of the sample while doing this step. Add a 50uL distilled water droplet and transfer grids membrane side down for 1 min wash. Remove excess fluid as explained before. Add 50uL of PBS on Parafilm and transfer grids membrane side down for a 3min wash, repeat x2 and remove excess fluid as mentioned before between washes. Add 50mM Glycine and transfer grids membrane side down for 3 minutes, repeat x4 and remove excess fluid in between. This is a blocking step. Transfer grids membrane side down to a 50uL droplet of 5% BSA in PBS for 10 min. Transfer grids membrane side down to a 5uL droplet of CD63 H5C6 anti-bodies (a 1:200 concentration of CD63 in 0.5% BSA in PBS) for 30min. Remove excess fluid as explained before. Transfer grids membrane side down to a 50uL droplet of PBS for a 3min wash, repeat x6 and remove excess fluid as explained before in between washes. Transfer grids membrane side down to a 50uL droplet of 0.5% BSA in PBS for a 3min wash, repeat x6 and remove excess fluid in between washes. Transfer grids to a 5uL droplet of Protein G (1:40 concentration in 0.5% BSA in PBS) for 120 min. Remove excess fluid as explained before and transfer grids membrane side down to a 50uL droplet of PBS for a 2min wash, repeat x8 and remove excess fluid in between washes. Transfer grids to a 50uL droplet of 1% GA for 1min for a post-fixing step. Transfer grids to a 50uL droplet of distilled water for a 2min wash, repeat x8 and remove excess fluid in between washes. Transfer grids membrane side down to a 50uL droplet of 2% UA for 10min. Air dry for 10min. Image in TEM at 80kV.

This process was optimized by reducing all washes to the technique explained in the whole mounted procedure. Also the GA post-fix was removed. Staining time was reduced from 10min to 10 seconds. The amount of washes was also reduced. We also increased the blocking time with BSA from x1 10min to x2 10min (before CD63 step).

Optimized Immunogold Labeling^{4,9}

Fix samples with 2% PFA for 20min. Then add 10uL of sample on clean Parafilm. Deposit the EM Formvar-carbon coated EM "holey grids" and let the grids adsorb the sample for 20min. Remove excess fluid by gently placing the membrane side of the grid on filter paper and quickly remove it, you should never let go of the sample while doing this step. Add a 50uL distilled water droplet and submerge grids membrane side down for a 3 second wash without releasing the grid. Remove excess fluid as explained before. Add 50uL of PBS on Parafilm and submerge grids membrane side down for a 3second wash. Add 50mM Glycine and submerge grids membrane side down for 3 seconds, repeat x3 and remove excess fluid in between, then transfer grid to 50uL drop for 4min. This is a blocking step. Transfer grids membrane side down to a 50uL droplet of 5% BSA in PBS for 10 min, repeat x2. Transfer grids membrane side down to a 5uL droplet of CD63 H5C6 anti-bodies (a 1:200 concentration of CD63 in 0.5% BSA in PBS) for 30min. Remove excess fluid as explained before. Submerge grids membrane side down to a 50uL droplet of PBS for a 3 second wash, repeat x4 and remove excess fluid as explained before in between washes. Transfer grids membrane side down to a 50uL droplet of 0.5% BSA in PBS for a 5min wash, repeat x2 and remove excess fluid in between washes. Transfer grids to a 5uL droplet of Protein G (1:40 concentration in 0.5% BSA in PBS) for 120 min. Remove excess fluid as explained before and

submerge grids membrane side down to a 50uL droplet of PBS for a 3 second wash, repeat x4 and remove excess fluid in between washes. Submerge grids to a 50uL droplet of distilled water for a 3 second wash, repeat x2 and remove excess fluid in between washes. Submerge grids membrane side down to a 50uL droplet of 2% UA for 10 seconds. Air dry for 10min. Image in TEM at 80kV.

Results and Discussion

Whole Mounted Procedure

The goal of the first experiment was to confirm that our samples had EV's in them. We define EV's as round- cup shaped morphology and in the size range from (40-500) nm (Exosomes and microvesicle)^{1,2,3,4,6}. As we can see on figure 1, we have EV's that perfectly fit this description. We then proceeded to optimize this procedure by essentially cutting time. The results of this was that we can effectively sample prepped and image the same. This is of great success since one purpose of this research was to find quick and accurate ways to image EV's. Figure 2 is a representative image of this optimization. We can observe that essentially the reduction in time didn't affect the quality of the image. We can actually see that we achieved better staining as comparing the vesicles from figure 1 are over stained.

Whole Mounted procedure with Methylcellulose⁴ (MC)

The purpose of adding methylcellulose to our procedure was to generate better background and contrast⁴. Based on our result we couldn't get a better background as we can see on Figure 3. But we did find an interesting application. Since we were using Formvar-carbon coated EM "holey grids", which are basically grids that contains hole on them as we can see in figure 4. The purpose of this grids is that sample should concentrate on the edges of the holes. Rather what we found was that the methylcellulose covered the holes and basically let us image in the holes. Essentially our EV's got stuck in the holes creating a very artefact free background as we can see in figure 5. The optimizations made to the process where helpful in the sense that the samples where quicker to make and essentially we can prepare samples and image the same day.

Immunogold Labeling^{4,9}

The purpose of Immunogold labeling was to further identify EV's by targeting CD63 membrane protein that EV's has been proven to contain³. We expected to find our EV's covered with the gold nanoparticles. As we can see from Figure 6, that was not the case. We can see that the gold nanoparticles where not binding specifically to our EV's, instead they seemed to be binding around them and in the background. To try and solve this problem, we increased our blocking, which purpose is to prevent unspecific binding. The results can be appreciated in Figure 7. We can see that we still didn't get the nanoparticles on our EV's but they seemed to be conglomerating around other stuff. We cannot called that other stuff EV's because they do not fit the previous description. We realized that our Protein G has some affinity to our blocking buffer, meaning that instead of binding to our CD63 H5C6 anti-body, they were binding to our BSA. Hence why they are conglomerating on the background and not our EV's.

Conclusion

The “Whole Mounted” procedure⁴ is a relatively simple, easy to do procedure that yields images where EV’s can be seen. Samples can be prepared and imaged the same day which is a great advantage for future biological research. The background is artefact free which means that images can be run through image processing programs to measure concentration and average size.

The methylcellulose procedures are also relatively simple and quick to do. Being able to image inside the holes of the “Holey Grids” is a very attractive concept since it’s background is artefact free which means that images can be run through image processing programs to measure concentration and average size. We have the same advantage as with “Whole Mounted” procedure in the sense that samples can be prepared and imaged the same day.

Immunogold Labeling stills need to be worked on since we didn’t get specific binding of nanoparticles to our EV’s. For future work is suggested to try a different blocking buffer since Protein G seems to have affinity with BSA. One possibility can be 1% cold-water fish skin gelatin (CFG) in PBS [They].

Acknowledgements

This work was supported by the Cornell Center for Materials Research with funding from the NSF MRSEC program (DMR-1120296). Also special thanks to Brian Kirby Ph.D., Frederick Theye, Jack Hartman, John Grazul and other members of Kirby Lab group.

References

1. Graca, R., & Stoorvogel, W. (n.d.). Extracellular vesicles: Exosomes, microvesicles, and friends. *The Journal Of Cell Biology*, 373-383.
2. Zhang, X., Yuan, X., Shi, H., Wu, L., Qian, H., & Xu, W. (n.d.). Exosomes in cancer: Small particle, big player. *Journal of Hematology & Oncology*, 1-13.
3. Melo, S. A., Luecke, L. B., & Kahlert, C. (n.d.). Glypican-1 identifies cancer exosomes and detects early pancreatic cancer. *Nature*, 1-24.
4. Theye, C., Clayton, A., Amigorena, S., & Graca, R. (n.d.). Isolation and Characterization of Exosomes from Cell Culture Supernatants and Biological Fluids. *Subcellular Fractionation and Isolation of Organelles*.
5. Erdbrugger, U., & Lannigan, J. (n.d.). Analytical Challenges of Extracellular Vesicle Detection: A Comparison of Different Techniques. *Cytometry Part A*, 1-12.

6. Pascucci, L., Cocce, V., Bonomi, A., Ami, D., & Ceccarelli, P. (2014, July 30). Paclitaxel is incorporated by mesenchymal stromal cells and released in exosomes that inhibit in vitro tumor growth: A new approach for drug delivery. *Journal of Control Release*, 262-270.
7. Van Der Pol, E., Hoekstra, A. G., Sturk, A., Otto, C., Van Leeuwen, T. G., & Nieuwland, R. (n.d.). Optical and non-optical methods for detection and characterization of microparticles and exosomes. *Journal of Thrombosis and Haemostasis*, 2596-2607.
8. Van Der Pol, E., Coumans, F. A., Grootemaat, A. E., Gardiner, C., Sargent, I. L., Harrison, P., . . . Nieuwland, R. (n.d.). Particle size distribution of exosomes and microvesicles determined by transmission electron microscopy, flow cytometry, nanoparticle tracking analysis, and resistive pulse sensing. *Journal of Thrombosis and Haemostasis*, 1182-1192.
9. Phillips, T. E., Ph.D. (n.d.). *Blocking Protocol LM/EM* (pp. 1-3, Rep.).

Figures

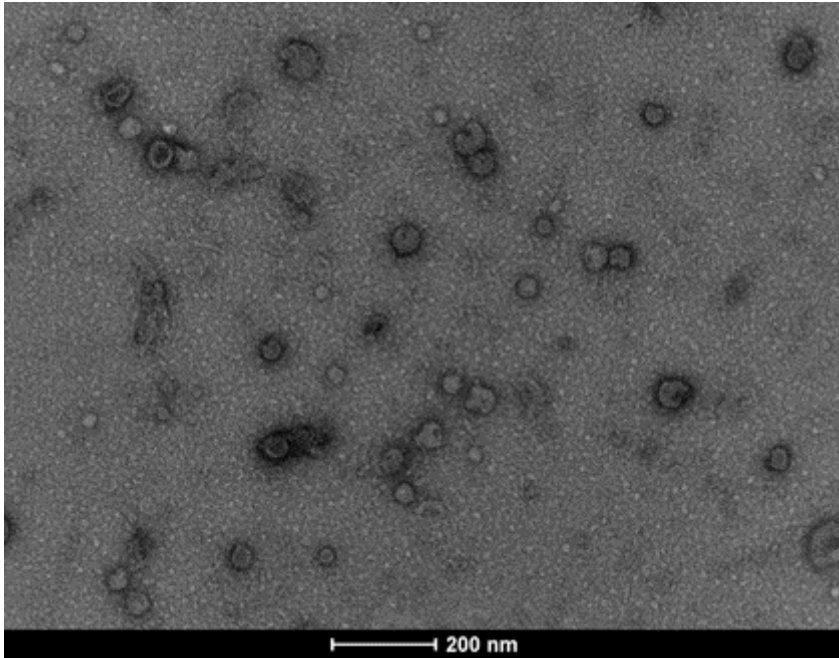


Figure 1. Image of EV's using the "Whole Mounted" procedure

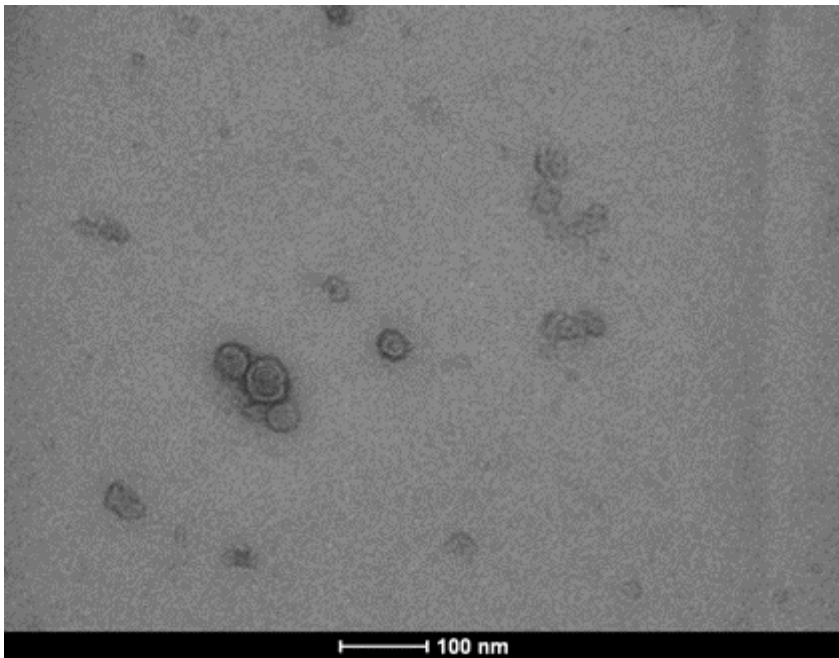


Figure 2. Image of EV's using the optimized "Whole Mounted" procedure

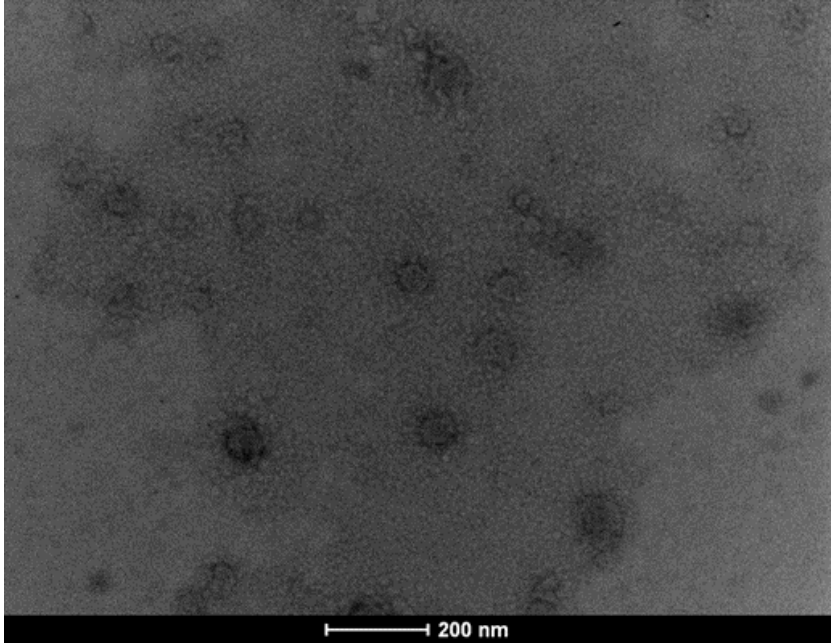


Figure 3. Image of EV's using the "Whole Mounted" procedure with MC

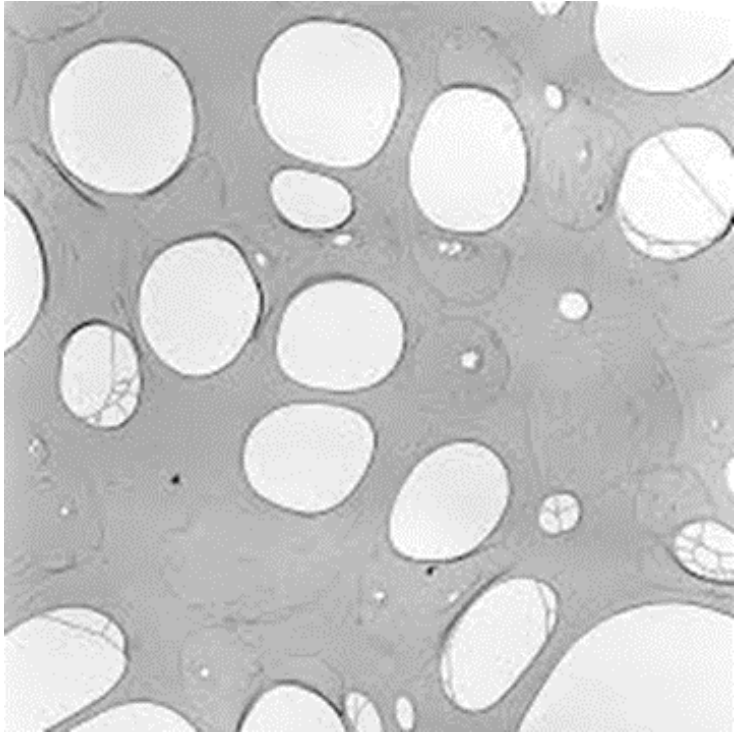


Figure 4. Image representative of "Holey Holes" present in EM Grids

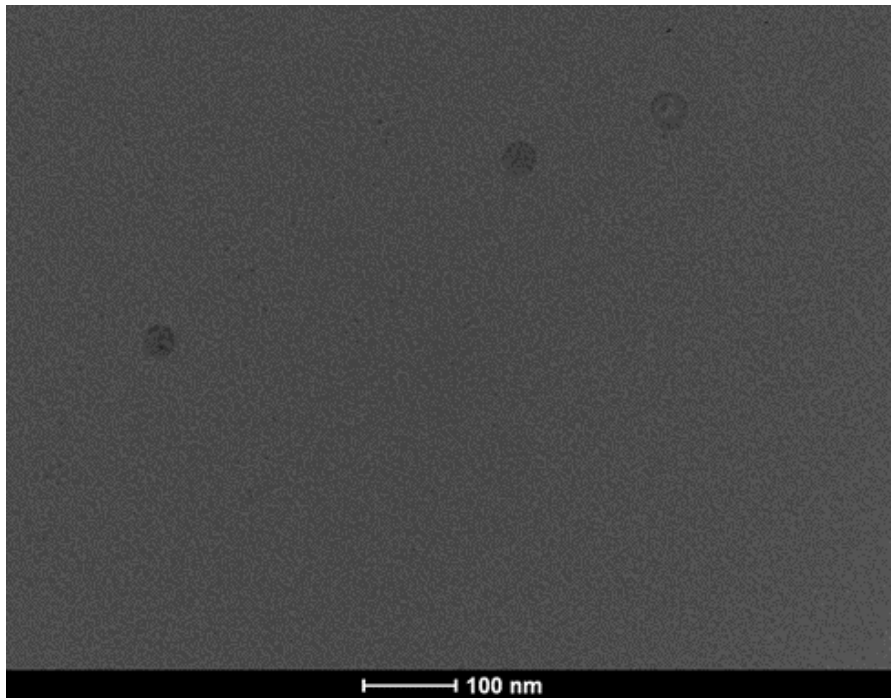


Figure 5. Image representative of “Whole Mounted” procedure with MC inside holes of “Holey Grids”

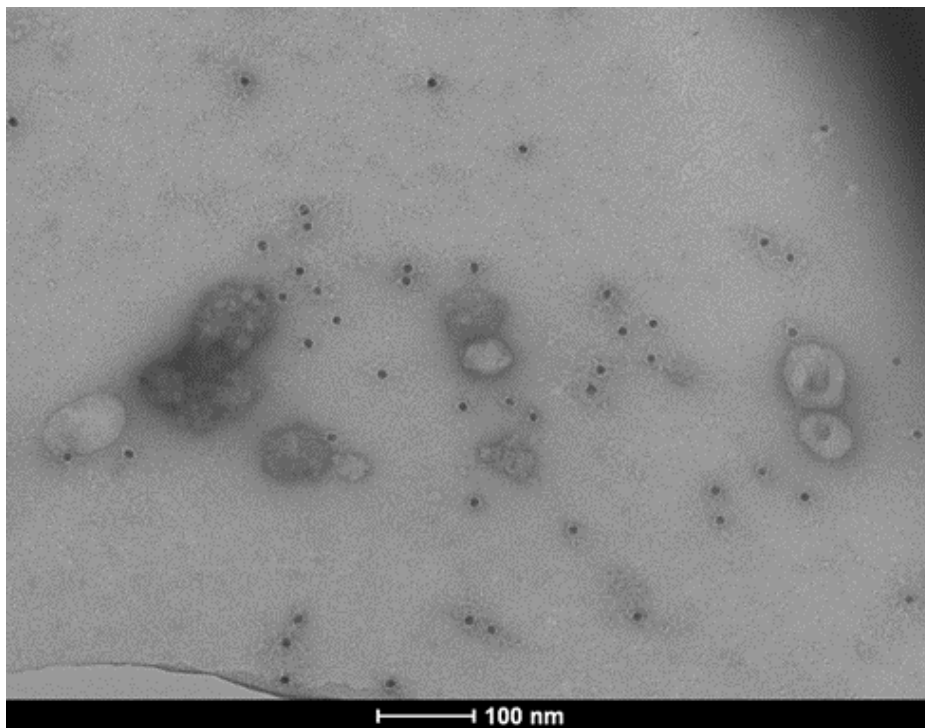


Figure 6. Image representative IGL process without optimization. We can appreciate unspecific binding of Protein G

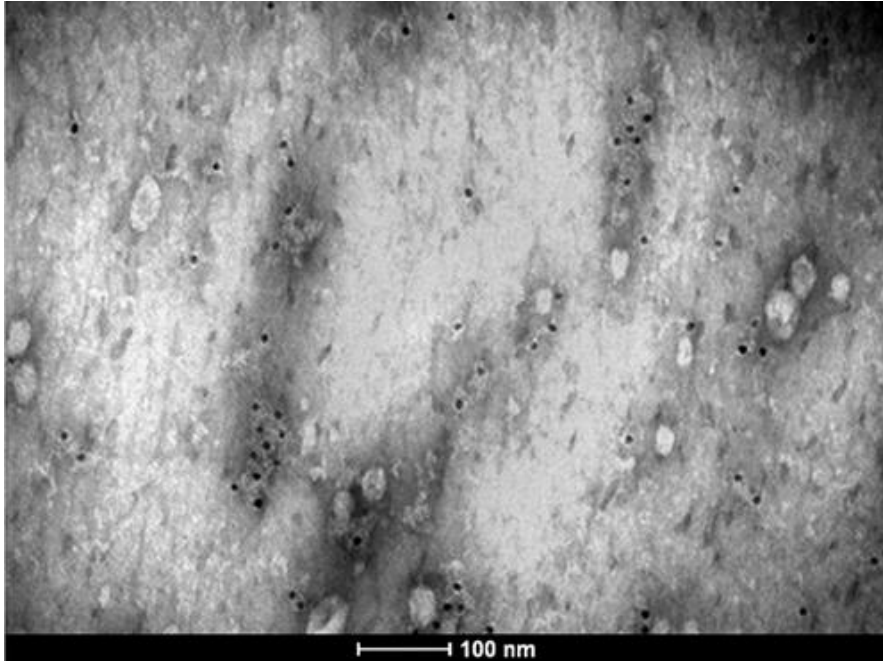


Figure 7. *Image representative of Optimized IGL process. We can see unspecific binding of Protein G but nanoparticle conglomeration on artefacts*

Micromagnetic Simulation of Constricted Spin-Hall Nano-Oscillators

Yanyou Xie, Albert Park, Emrah Turgut, Gregory D. Fuchs*
 Cornell Center for Materials Research
 Cornell University, Ithaca, New York, U.S.A. 14853
 (Dated: August 10, 2016)

We present a new design of constricted spin-Hall nano-oscillators in this project. Simulations were carried out and compared with experimental measurements. We studied the dependence of oscillation frequencies on applied magnetic field and current for (1) CoFeB ferromagnetic layer only and (2) ferromagnetic layer with spin-Hall induced spin-transfer torque (STT). The modes at peak frequencies at the central region of the ferromagnetic layer were also studied, with both the bulk modes and edge modes identified.

I. INTRODUCTION

Nano-oscillators may be used as future microwave sources for wireless communications with the advantages of miniature size and fast switching speed [1]. Ferromagnetic materials can act as a major component in nano-oscillators because of their intrinsic ability to oscillate. When an external magnetic field \mathbf{H} is applied at an angle with the magnetization \mathbf{M} of the ferromagnetic material, a torque will be generated, driving the magnetization to precess around magnetic field with damping, as shown in Figure 1. The evolution of magnetization follows Landau-Lifshitz-Gilbert equation

$$\frac{d\mathbf{M}}{dt} = -\gamma_0 \mathbf{M} \times \mathbf{H}_{eff} + \frac{\alpha}{M_S} \mathbf{M} \times \frac{d\mathbf{M}}{dt}, \quad (1)$$

where γ is the gyromagnetic ratio for an atomic spin, α is the dimensionless Landau damping constant and \mathbf{H}_{eff} is the effective magnetic field (T) [2]. The second term in the right hand side of the equation is a damping term.

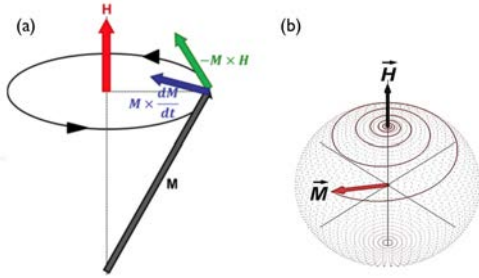


FIG. 1. (a) Torque components exerted on the magnetization \mathbf{M} by rotational field \mathbf{H} (b) Motion of \mathbf{M} for constant \mathbf{H} [3].

To sustain a stable oscillation, a spin-transfer torque (STT) in the opposite direction is required to compensate the damping term. This torque results from the transfer of angular momentum from a spin-polarized charge current or a pure spin current to a local magnetization [1].

The stable oscillations due to STT is called auto-oscillations. Currently, magnetic auto-oscillations could be observed in two groups of devices: spin-transfer nano-oscillator and spin-Hall nano-oscillators (STNOs and SHNOs) [1]. An example for each type of nano-oscillators is shown in Figure 2.

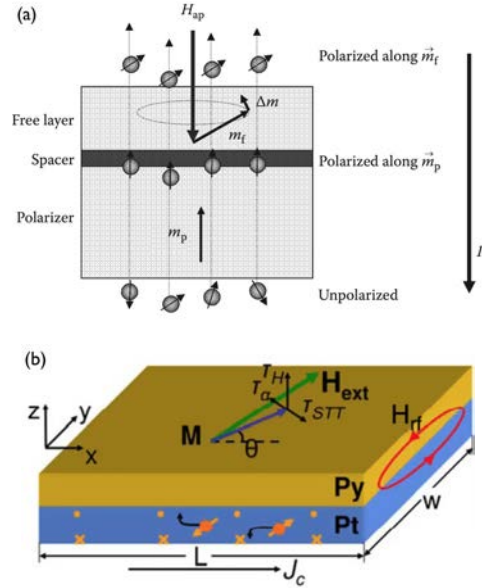


FIG. 2. (a) An ferromagnet/spacer/ferromagnet trilayer STNO [4] (b) An SHNO design, where Pt is the spin-Hall layer and Py is ferromagnetic layer [5].

STNOs usually have a trilayer structure consisting of two ferromagnetic layer and a spacer layer in between. One ferromagnetic layer with fixed magnetization acts as a polarizer, while the other ferromagnetic layer has free magnetization which can rotate in response to the spin transfer torque [4]. As shown in Figure 2, the electrons are polarized along \mathbf{m}_p after passing through the fixed layer. When the electrons try to align their spin with the polarization in free layer \mathbf{m}_f , the spin momentum is transferred to the free layer magnetization [4]. Here \mathbf{m} is the normalized magnetization where $\mathbf{m} = \mathbf{M}/M_s$.

In contrast, SHNOs often adopt a bilayer structure – a non-magnetic spin Hall layer and a ferromagnetic free

* a0119537@u.nus.edu, amp356@cornell.edu, turgut@cornell.edu, gdf9@cornell.edu.

layer. SHNOs utilize the spin Hall effect, which causes electrons with different spins flowing in a heavy metal to split, generate a transverse pure spin current [1, 5–7]. The spin current can then induce a STT in the adjacent ferromagnetic layer and thus allow auto-oscillation of the SHNO.

The current problems for STNOs and SHNOs are their low output power and large linewidth, and an possible path to solve both problems is to synchronize among nano-oscillators [1]. Therefore, it is helpful to develop new geometries of nano-oscillators that are able to synchronize. Our group has developed several SHNO constricted nanowires with novel geometries. The presented simulations aim to explore the dependence of frequency on applied magnetic field and current, as well as the modes for (1) the ferromagnetic layer only (2) the ferromagnetic layer in a SHNO.

II. METHODS

MuMax³ micromagnetic simulation package was used for all the simulations [8]. The Landau-Liftshitz torque, described by Equation 1, and Slonczewski spin-transfer torque were included in the simulation. The Slonczewski STT was used to simulate the STT generated by spin Hall effect. The revolution of the normalized magnetization was recorded, both as a spatially-averaged magnetization over the whole sample and as individual magnetization for each cell.

The top-view of the geometries of the constricted nanowires for simulations are included in Figure 3. The distance between the end constrictions is 1800 nm for all three geometries. The width of the constriction is 200 nm and the width of the widest point is 800 nm for all three geometries. The thickness of the CoFeB ferromagnetic layer and the spin-Hall Pt layer are each 4 nm.

The simulated region has a dimension of $5800 \times 4000 \times 4$ nm. For the material parameters, we used $A_{ex} = 10^{-11}$ J/m for exchange stiffness, $M_s = 1.3 \times 10^6$ A/m for saturation magnetization. Two stages of simulations were carried out, namely

- (1) Simulation of ferromagnetic layer only
- (2) Simulation of ferromagnetic layer in a SHNO

For (1), a constant magnetic field was applied in y direction, and a Gaussian pulse was sent in x direction after some time, triggering an oscillation. Without the STT, the damping will reduce the amplitude of the oscillation until the oscillation ceases. This process is also called the “ringdown” of micromagnetics. To observe more long-lasting oscillation, a small damping constant $\alpha = 0.002$ was used. Simulations were also carried out for different constant magnetic fields.

For (2), the STT is induced by the spin Hall effect, which we were unable to directly simulate in MuMax³. Therefore, we calculated the spin current and then applied the resultant current in similar way as the Slon-

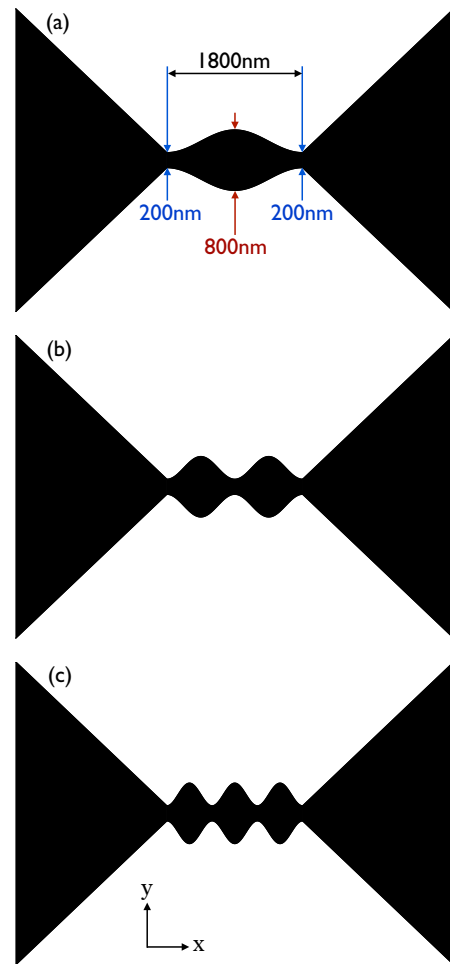


FIG. 3. Top-view nanowire geometries for (a) 2 constrictions (b) 3 constrictions (c) 4 constrictions

czewski STT. In SHNO, the charge current is applied in plane. Therefore, the CoFeB layer and Pt layer can be viewed as connected in parallel. The proportion of charge current passing through the Pt layer was calculated using the resistivity of both materials – $\rho_{\text{CoFeB}} \approx 170 \mu\Omega\cdot\text{cm}$ [6] and $\rho_{\text{Pt}} = 10.6 \mu\Omega\cdot\text{cm}$ [9]. The proportion of spin current generated was further calculated using the spin Hall angle of Pt $|\theta_{SH}^{\text{Pt}}| \approx 0.07$ [6]. The damping constant used in this stage was $\alpha = 0.008$ [6, 10, 11]. In our case, the charge current is applied in x direction, with a constant magnetic field applied in y direction. Simulations for different charge currents were carried out.

After each simulation, the discrete Fourier transformation was used to analyze the recorded magnetization versus time. The peak frequencies of oscillations were identified and modes of the corresponding frequencies were plotted using *Mathematica*.

III. DATA AND ANALYSIS

III.1. Ringdown Micromagnetics

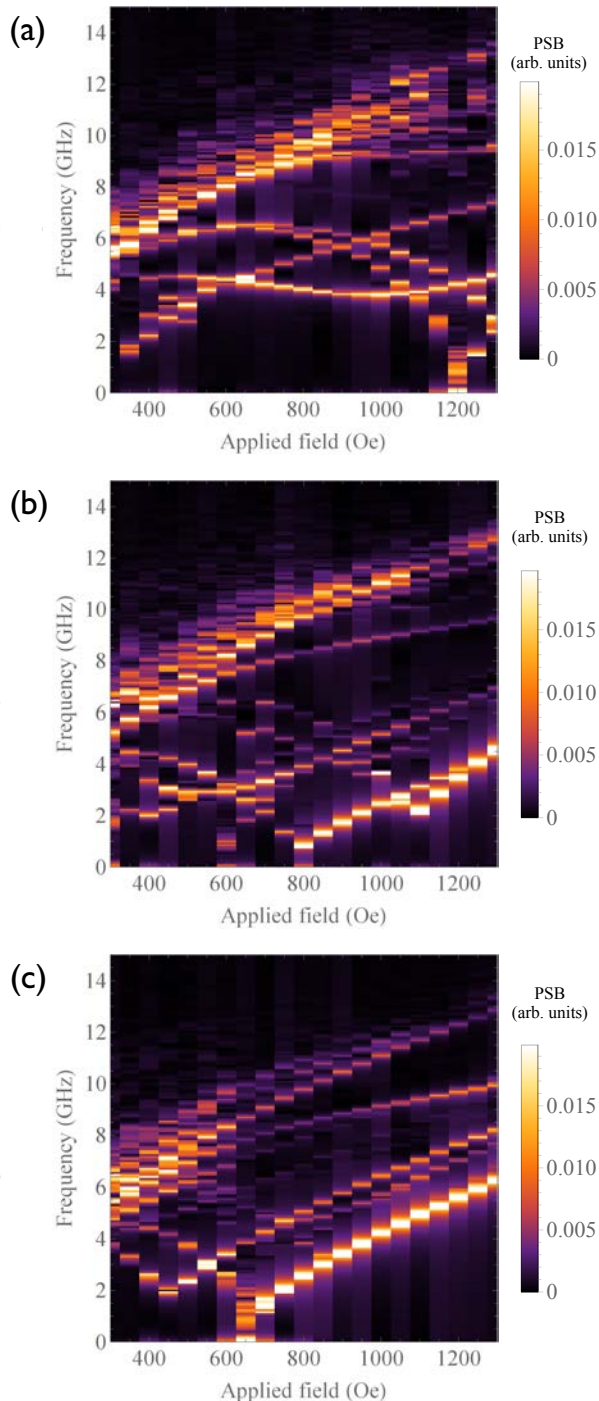


FIG. 4. Spectrum of discrete Fourier transformation peaks at different applied magnetic field for: (a) the 2-constriction wire in Figure 3(a) (b) the 3-constriction wire in Figure 3(b) and (c) the 4-constriction wire in Figure 3(c). The intensity of the peaks are normalized along each applied field. The power spectrum density is indicated by the legend.

In those simulations where only the ferromagnetic layer was involved, the peak frequencies generally increased with applied magnetic field except for few odd lines, as shown in Figure 4. There are more than one peak frequencies at each applied field. It was obvious that there are a general trend from around 6 GHz at 300 Oe to around 13 GHz at 1300 Oe for all three geometry ferromagnetic nanowires. Moreover, below the general trend there were several outlier lines, most of which were in V-shape. These outlier lines shift position when the number of constriction in the nanowire increases.

Further exploration of the modes at the peak frequencies reveals that the modes along the general trend are bulk modes (as in Figure 5(a)) while those outside of the general trend are edge modes (as in Figure 5(b)). For a specific nanowire geometry, each outlier lines represented one mode. When more than one lines intersected, the mode at the intersection had the characteristic of modes on both lines. It is observed that at lower applied magnetic field, the peaks for bulk modes have larger intensity than those for edge modes. However, at higher applied magnetic field, the peaks for edge modes dominates, especially in the 4-constriction nanowire.

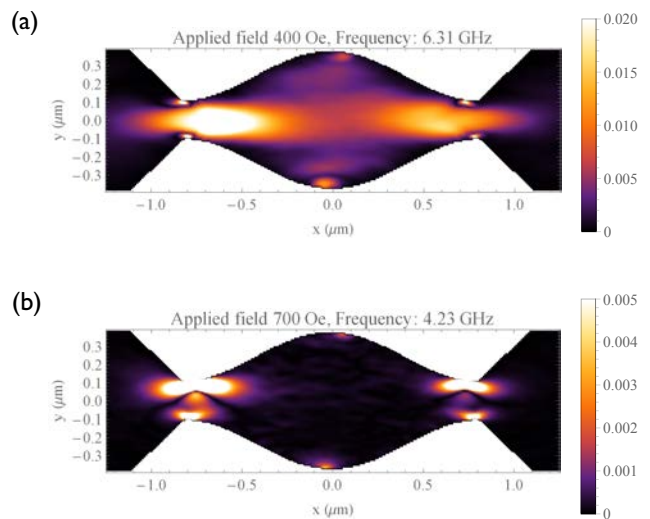


FIG. 5. (a) A sample bulk mode (b) A sample edge mode

The spectrum from simulation were also compared with the spectrum from ferromagnetic resonance (FMR) experimental data, as shown in Figure 6. The simulation and experimental results agreed quite well, especially for the 2-constriction nanowire.

III.2. Spin-Hall Auto-oscillation

The effect of Spin-Hall layer was taken into account during the second stage of simulation. Under appropriate conditions (charge current and applied magnetization), there were auto-oscillations in the z direction, as shown in

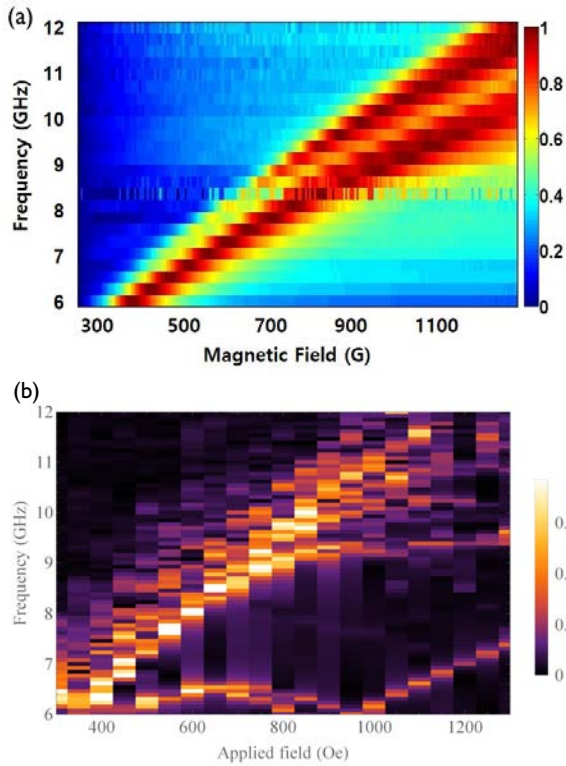


FIG. 6. Comparison between spectrums from (a) experimental data (b) simulation

Figure 7. The corresponding mode is shown in Figure 7. The oscillations sometimes experience a transient stage at the early time range of the simulation where the frequency of the oscillation have not been stabilized. When applying a different charge current, a different mode may occur, as in Figure 8. Compared with Figure 5, the mode in Figure 7 looks more similar to an edge mode, while the mode in Figure 8 is akin to a bulk mode. Also it is noted that the modes were asymmetric along y axis. Further exploration on the modes may be required.

Moreover, from Figure 9 we observed the dependence of frequency on current at a fixed magnetic field. If the current applied is too small, the oscillations could not be sustained and damping occurs. When the current increased to 1.5 mA, there was auto-oscillation as shown in Figure 7. However, the intensity of the peaks between 1.5-1.8 mA were extremely small compared to their counterparts between 1.9-3 mA. The line represent peaks between 1.5-1.8 mA is barely visible in Figure 9. In contrast, there is a line clearly indicating the peaks between 1.5-1.8 mA in the same figure. It was observed that the peak frequencies in this region does not change much with respect to the charge current applied. The peak with highest intensity occurs at 2.5 mA.

We further studied the dependence of peak frequency on applied magnetic field when applying a charge current of 2.5 mA, as shown in Figure 10. Only a single peak frequency was observed for each applied magnetic field.

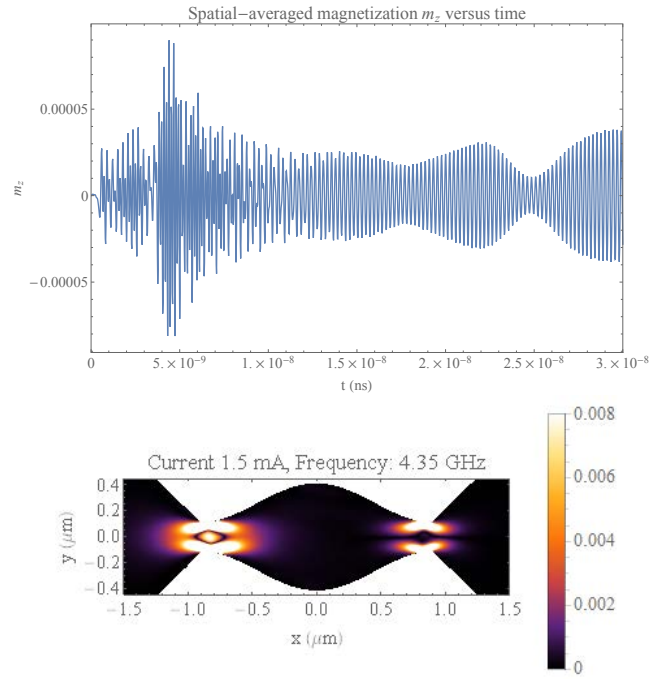


FIG. 7. Auto-oscillation of m_z over time at 500 Oe for nanowire of 2 constrictions, with a total current of 1.5 mA, and the corresponding mode at the peak 4.35 GHz

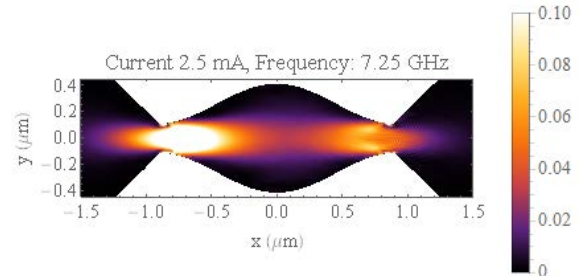


FIG. 8. Mode at the peak 7.25 GHz when applied field is 500 Oe for nanowire of 2 constrictions, with a total current of 2.5 mA

The peak frequency increases monotonously with applied field. By comparing Figure 10 with Figure 6 we found that the spectrum for spin-Hall auto-oscillation exhibits similar trend to the spectrum for FMR and ringdown micromagnetic simulation. By studying the corresponding modes to the peak frequencies in Figure 10, we found that these modes are all bulk mode, similar to the one shown in Figure 8.

The nanowires of with 2 constrictions may act as a SHNO and it can be tuned over a range of frequencies by applying different magnetic field. Due to time constraint, only the results from the 2-constriction nanowire were included in this report. Further work may be done to study the spectra and modes for 3-constriction and 4-

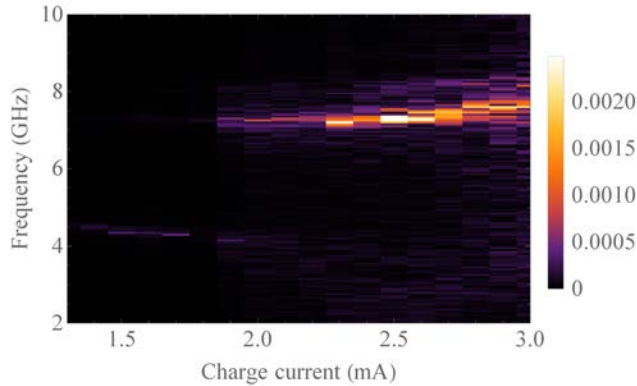


FIG. 9. Spectrum of discrete Fourier transformation peaks at 500 Oe when applying different charge current in the 2-constriction nanowire

constriction nanowires, as well as to carefully study the possible phase-locking at the constrictions.

IV. CONCLUSIONS

In conclusion, during the simulation of ringdown micromagnetics, we found the spectra for nanowires with different number of constrictions and we identified the bulk and edge modes. The simulation gave similar results to the experiment. After that, we simulated Spin-Hall effect driven auto-oscillations and observed auto-oscillations after applying the current. The modes at each peak frequencies were identified for different cur-

rent levels. Further work may be done for the geometries with different number of constrictions and also to identify possible phase-locking at the constrictions.

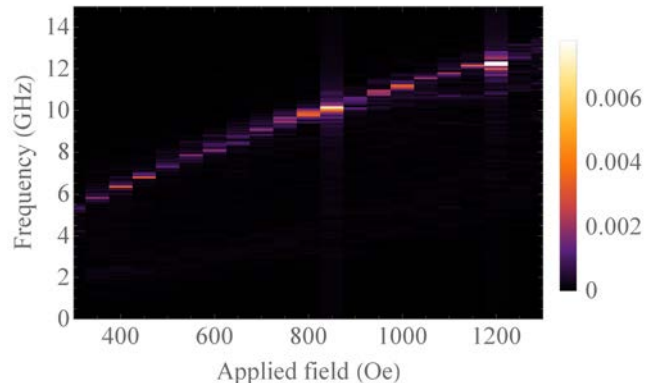


FIG. 10. Spectrum of discrete Fourier transformation peaks 2.5 mA when applying different magnetic field to the 2-constriction nanowire

ACKNOWLEDGMENTS

I would like to express my gratitude to Professor Gregory Fuchs for his patient guidance and enthusiastic encouragement during the research project. Thanks to Albert Park and Dr. Emrah Turgut for the assistance with MuMax³ and *Mathematica*. My participation would not have been possible without the collaboration of American Chemical Society with Cornell Center for Materials Research.

-
- [1] T. Chen, R. K. Dumas, A. Eklund, P. K. Muduli, A. Houshang, A. A. Awad, P. Dürrenfeld, B. G. Malm, A. Rusu, and J. Åkerman, “Spin-torque and spin-hall nano-oscillators,” *arXiv preprint arXiv:1512.03162*, 2015.
 - [2] D. Wei, *Maxwell Equations and Landau-Lifshitz Equations*, pp. 21–52. Berlin, Heidelberg: Springer Berlin Heidelberg, 2012.
 - [3] M. Sharma, S. Pathak, and M. Sharma, *Ferromagnetic Resonance—Theory and Applications*, ch. 4. FMR Measurements of Magnetic Nanostructures, pp. 93–110. In-Tech, 2013.
 - [4] S. E. Russek, W. H. Rippard, T. Cecil, and R. Heindl, *Handbook of Nanophysics: Functional Nanomaterials*, ch. 38. Spin-Transfer Nano-Oscillators, pp. 38–1 – 38–23. Handbook of Nanophysics, CRC Press, 2010.
 - [5] L. Liu, T. Moriyama, D. Ralph, and R. Buhrman, “Spin-torque ferromagnetic resonance induced by the spin hall effect,” *Physical review letters*, vol. 106, no. 3, p. 036601, 2011.
 - [6] L. Liu, C.-F. Pai, Y. Li, H. W. Tseng, D. C. Ralph, and R. A. Buhrman, “Spin-torque switching with the giant spin hall effect of tantalum,” *Science*, vol. 336, no. 6081, pp. 555–558, 2012.
 - [7] J. Sinova, S. O. Valenzuela, J. Wunderlich, C. Back, and T. Jungwirth, “Spin hall effects,” *Reviews of Modern Physics*, vol. 87, no. 4, p. 1213, 2015.
 - [8] A. Vansteenkiste, J. Leliaert, M. Dvornik, M. Helsen, F. Garcia-Sanchez, and B. Van Waeyenberge, “The design and verification of mumax3,” *AIP Advances*, vol. 4, no. 10, 2014.
 - [9] J. Agustsson, U. Arnalds, A. Ingason, K. B. Gylfason, K. Johnsen, S. Olafsson, and J. Gudmundsson, “Electrical resistivity and morphology of ultra thin pt films grown by dc magnetron sputtering on sio2,” in *Journal of Physics: Conference Series*, vol. 100, p. 082006, IOP Publishing, 2008.
 - [10] X. Liu, W. Zhang, M. J. Carter, and G. Xiao, “Ferromagnetic resonance and damping properties of cofeb thin films as free layers in mgo-based magnetic tunnel junctions,” *Journal of Applied Physics*, vol. 110, no. 3, 2011.
 - [11] K. Buschow, ed., *Handbook of Magnetic Materials*. No. v. 21 in Handbook of Magnetic Materials, Elsevier Science, 2013.

ORR Electrocatalysts and Alkaline Anion Exchange Membrane Assembly for Enhanced Fuel Cell Performance

Geraldine Marin-Zamora^{#*}, Johary Rivera-Meléndez^{*}, Abigail Van Wassen^{*} and Héctor D. Abruña^{*}

[#]Department of Chemistry, University of North Carolina-Chapel Hill, Chapel Hill, North Carolina 27599

^{*}Department of Chemistry and Chemical Biology, Baker Laboratory, Cornell University, Ithaca, New York 14853

Abstract

With the development of cationic, hydroxide-conducting alkaline anion exchange membranes (AAEMs), alkaline fuel cells are becoming a feasible alternative to traditional acidic fuel cells. Working in alkaline medium enables the use non-precious metals as catalysts for the oxygen reduction reaction (ORR) taking place at the cathode. From previous work of past Abruña-group members, Pd_xCu_y was found to be a promising, less expensive (than Pt) catalyst for this reaction. We have tested various compositions of sputtered metal thin film Pd_xCu_y electrodes with a 300 nm thick AAEM layer, (synthesized at Cornell University by the Coates group), to further study a more realistic cathode membrane (assembly) interface and gain a deeper understanding of the processes taking place at the various interfaces. For electrochemical characterization, we employed the rotating disk electrode (RDE) voltammetry method in a three-electrode electrochemical cell using 0.1M NaOH as the electrolyte solution. Our results of the best Pd_xCu_y composition, in terms of onset potential, were consistent with previous findings prior to incorporating the AAEM. However, the limiting current was affected unfavorably when the membrane was applied, suggesting transport limitations.

1. Introduction

Worldwide, scientists are investigating alternative ways to develop energy generation and conversion technologies in an effort to be lessen our dependency on fossil fuels and lower carbon

dioxide emissions into the environment. Fuel cells can cleanly and efficiently convert chemical energy from hydrogen (and other fuels) into electrical energy, while generating virtually no pollutants. Fuel cells operating in alkaline media rather than acidic media, enable the use of non-precious metals to catalyze the oxygen reduction reaction (ORR) and thereby increase efficiency and lower the cost of the overall device. With the discovery of lower cost binary and ternary metal alloys to inexpensively catalyze the ORR reaction and the development of anion exchange membranes (AAEMs), alkaline fuel cells are becoming an attractive option to replace the existing, acid based, fuel cell technologies in vehicles.

A fuel cell is composed of an anode, a cathode, and an electrolyte layer in between. At the anode, fuel oxidation (hydrogen or other) takes place while the oxygen reduction reaction (ORR) occurs at the cathode. The ORR's slow kinetics, resulting in very high overpotentials, has hindered the widespread deployment of this technology. Abby Van Wassen's work (in the Abruña group) on metal binary thin films in alkaline media has shown strong ORR electrocatalytic activity in palladium-copper compositions¹. The alkaline anion exchange membrane, synthesized by the Coates group at Cornell University, is comprised of a polymer backbone and has cationic sites to effectively conduct negatively charged species, in this case hydroxide ions. We performed analytical studies on various Pd_xCu_y compositions with a 300 nm thick AAEM to further study and characterize the activity of these electrocatalysts cationic-membrane interfaces.

2. Experimental Section

2.1. Preparation of Ionomer Modified Pd_xCu_y Thin Film Electrodes

Polymer samples with a 1:2.5 ratio of functional to structural components (Figure 1) were prepared as reported previously [2]. The polymer was synthesized in the Cl⁻ form and was ion-exchanged to the OH⁻ form by immersing the sample in 1.0 M NaOH solution and stirring for 20 minutes. This procedure was repeated three times, changing to a fresh solution of base after 20 minutes, to ensure complete displacement of Cl⁻ by OH⁻. Subsequently, the sample in the OH⁻ form was immersed in 1.0 M Na₂CO₃. A complete conversion of the polymer to the CO₃²⁻ form eliminates potential degradation of the polymer due to nucleophilic attack by OH⁻. To ensure complete removal of any residual OH⁻ and CO₃²⁻, the samples were soaked in DI water for 20_min. This process was repeated twice. The polymer, in the CO₃²⁻ form, was left drying overnight between two sheets of tissue paper to remove any excess water. The dried sample was weighed accordingly to obtain a 1.0 wt % in the final ionomer solution. A prescribed volume of n-propanol was added to the sample, in a sealed capped vial with a stir bar, and left stirring at room temperature until the polymer dissolved completely.

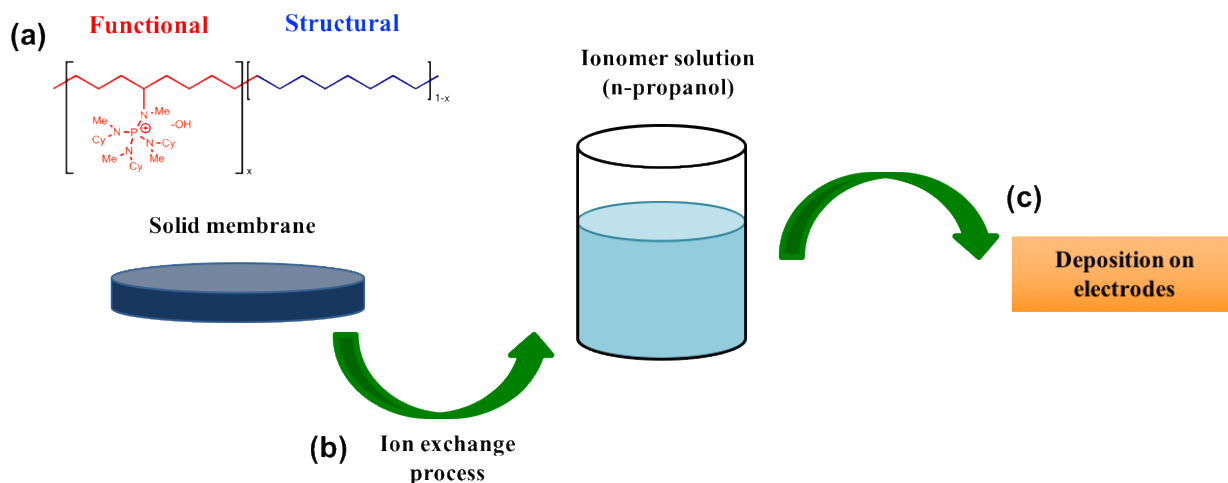


Figure 1. (a) Chemical structure of phosphonium AAEM (b) Ion exchange process (c) Deposition on electrodes

The RDE setup consisted of a rotator equipped with a control unit (Pine Model AFMSRX). The RDE electrodes were disks (5 mm in diameter) of glassy carbon modified with thin films of different PdCu compositions. They were inserted into the change disk type RDE tips (Pine E4QT Series ChangeDisk RDE tips). The change disk type tips allow the electrodes to be removed out of the tip for further characterization using other methods. The AAEM ionomer thin films were deposited on the RDE electrodes by employing the rotator as a spin-coater. For this purpose, the rotator assembly was mounted upside down on the support pillar. The rotator shaft (with the RDE electrode unit mounted) was then inserted into the rotator assembly such that the exposed face of the RDE electrode was facing up. An aliquot of 20 μL of the ionomer solution was then introduced on to the stationary electrode and subsequently the electrode rotated at a speed of 1,000 rpm for 5 minutes.

To verify that the appropriate film thickness was achieved, a Tencor Alpha Step 500 contact profilometer was used. Step edges were created on identically prepared samples using a pointed swab that was previously submerged in n-propanol. An average of the lines was used to determine the thickness of the spin-coated film.

2.2. Oxygen Reduction Reaction

A custom built three-electrode electrochemical cell was used for the RDE experiments. A high surface area Pt wire and a saturated Ag/AgCl (BASi) were used as counter and reference electrodes, respectively. The various 5 mm glassy carbon slugs with Pd_xCu_y sputtered films were inserted into the interchangeable RDE electrode assembly and into the shaft along with a glass cap to maintain an oxygen atmosphere during rotation. The rod was inserted into the RDE rotator (Pine Research Instrumentation, AFMSR).

The electrochemical cell was filled with 50 mL of 0.1 M NaOH electrolyte solution for testing. Prior to experimentation, the solution was purged with nitrogen gas for 15 minutes to remove any residual gases. Afterwards, the electrode was electrochemically cleaned by cycling the potential from -0.6 to +0.3 V vs. Ag/AgCl at a scan rate of 50 mV/s until the cyclic voltammetric response no longer changed. The nitrogen gas was switched to oxygen gas for 15 minutes and rotating disk electrode experiments were performed at a scan rate of 20 mV/s and at rotation rates ranging from 50-2000 rpm. After each rotation, the cell and electrolyte solution were purged with oxygen gas for 7 minutes.

2.3. Data Analysis:

The data collected were analyzed through the Levich equation (Equation 1). The number of electrons involved in the reaction was determined setting the D_0 (diffusion coefficient) and concentration of oxygen (O_2) to be $1.93 \times 10^{-5} \text{ cm}^2\text{s}^{-1}$ and 1.25 mM, respectively. The Levich analysis was performed on the mass-transport limited currents at the specified rotation rates.

3. Equations

In rotating disk electrode voltammetry, the number of electrons that are involved in a redox reaction can be obtained from the Levich equation

$$i_l = -0.62nFAD^{2/3} \omega^{1/2} \nu^{-1/6} C \quad (1)$$

where i_l is the limiting current at a given rotation rate (ω), n is the number of electrons transferred, F is Faraday's constant, A is the electrode area (cm^2), D is the diffusion coefficient of the redox active species (cm^2/s), ω is the electrode rotation rate (rad/s), ν is the kinematic viscosity (cm^2/sec) and C is the solution concentration of the redox active species (mol/cm^3). For

the analysis of O₂, we used the diffusion coefficient of 1.93 x 10⁻³ cm²/s, determined by *Blizanac et al.*² The Levich equation is valid when the system is mass-transport limited at all rotation rates and this is evidenced by the linearity of the Levich plot (*i*_l vs. $\omega^{1/2}$).

4. Results and Discussion

We tested compositions from Pd₁Cu₉ to Pd₉Cu₁ at 10% increments with a 300 nm thick AEEM layer, and the recorded voltammetric profiles were compared. Many of the profiles had overlapping regions, but compositions containing more palladium than copper had smoother voltammetric profiles and higher onset potentials. For easier interpretation, we compared a palladium-rich electrode, a copper-rich electrode, and an electrode that had equal parts palladium and copper (Figure 2).

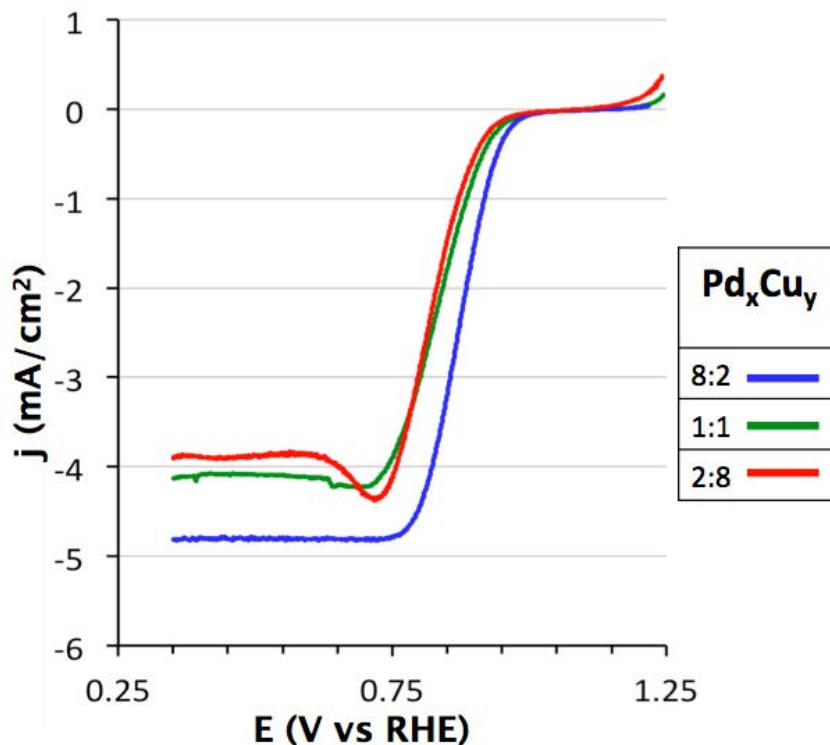


Figure 2. Metacomparison of different compositions tested: Pd₈Cu₂, Pd₁Cu₁ Pd₂Cu₈ with a 300 nm thick AAEM layer. Rotation rate, 1500 rpm in 0.1 M NaOH. $v = 20\text{mV/s}$

As can be seen, the palladium-rich compositions had more positive onset potentials. This is expected due to the high activity of palladium as an electrocatalyst for the ORR, relative to copper. While the Pd₈Cu₂ composition exhibited the highest activity, it was also the most expensive. Performance and cost are key factors/metrics when selecting an electrocatalyst. By combining palladium and copper, we hoped to achieve good catalytic activity/performance, related to both kinetics and mechanism, and cost.

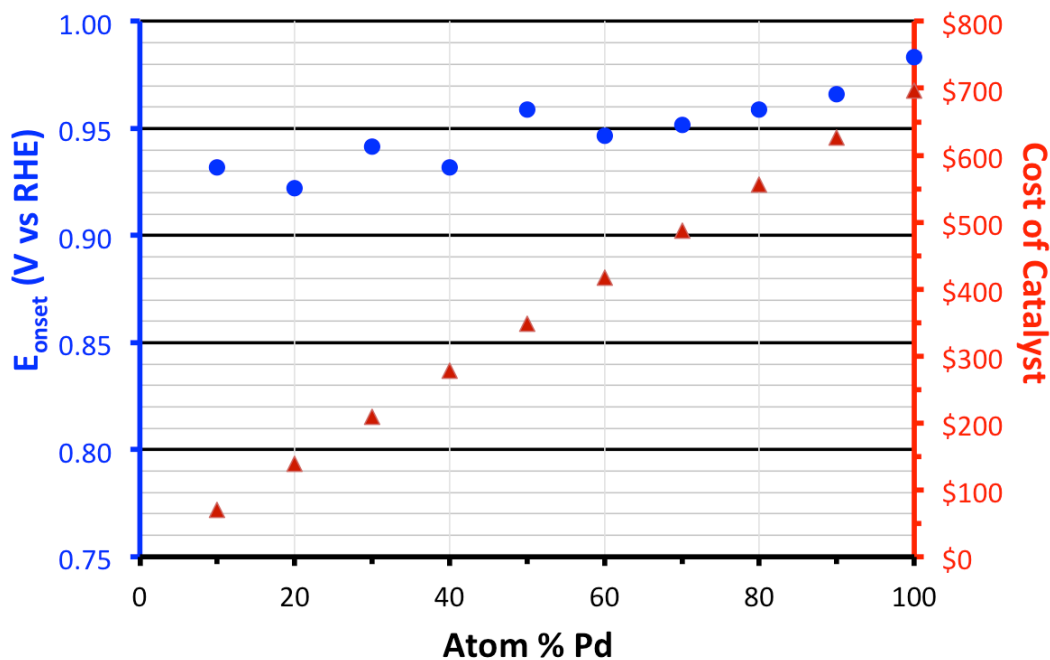


Figure 3: E_{onset} and catalyst cost as a function of Pd content. Points were determined at a rotation rate of $\omega = 350$ rpm at 20 mV/s in 0.1 M NaOH.

After characterizing each composition with regards to onset potential and cost, the optimal composition was determined to be Pd₁Cu₁. It had an onset potential virtually identical to that of a palladium rich electrode, while significantly decreasing the price. Note, that the cost in Figure 3 is solely the cost of the electrocatalyst and does not include the cost of the membrane, which would be constant for all electrocatalyst compositions. To test the effects of the membrane, we compared the cathodic (negative-going) sweeps of the Pd₁Cu₁ electrode with and without the membrane (Figure 4).

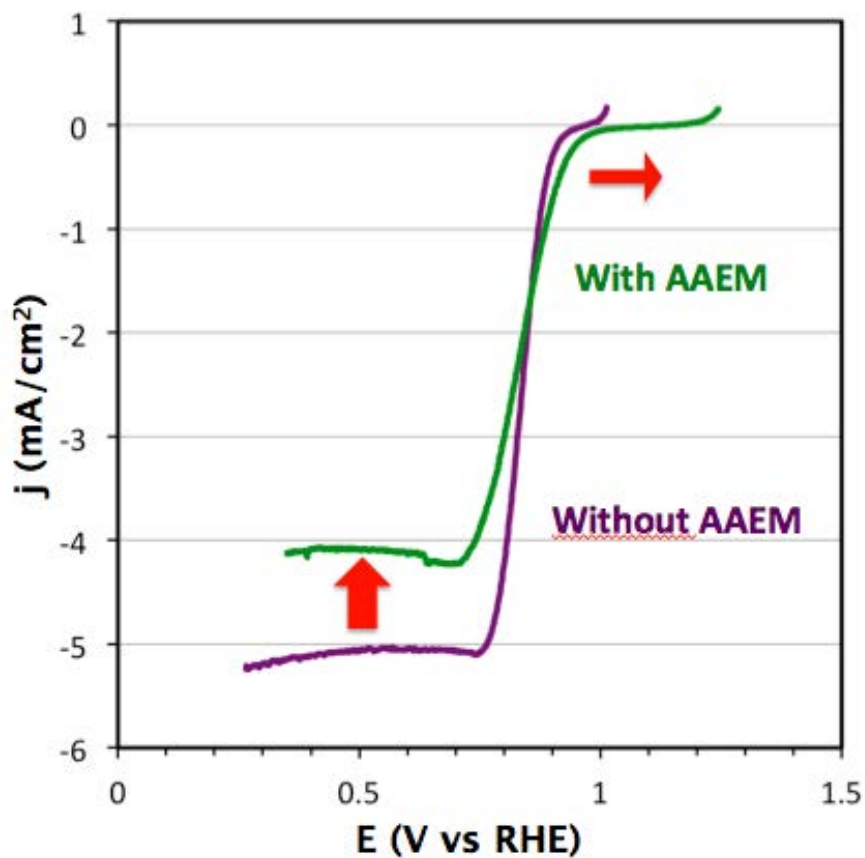


Figure 3. Comparison of Pd₁Cu₁ ORR electrocatalytic activity with and without the AAEM membrane. 1500 rpm in 0.1 M NaOH. $v = 20\text{mV/s}$

Interestingly, the onset potential was more positive on the electrode with the membrane, perhaps due to a binding property of the membrane or to a high partition coefficient for oxygen, resulting in an effectively higher initial concentration of oxygen. This increase in onset potential is desired, since it means it has a lower overpotential, requiring less energy to drive the oxygen reduction reaction. However, the membrane also decreased the limiting current of the electrode. This could be due to transport inhibiting effects of the membrane for oxygen to reach the surface of the electrode.

We used the limiting current data of the Pd₁Cu₁ electrode, with and without the AAEM, and used the Levich equation to determine the number of electrons transferred (Figure 5). The electrode with the membrane had a 1.66 electron count, while the electrode without the membrane had a 3.42 electron count.

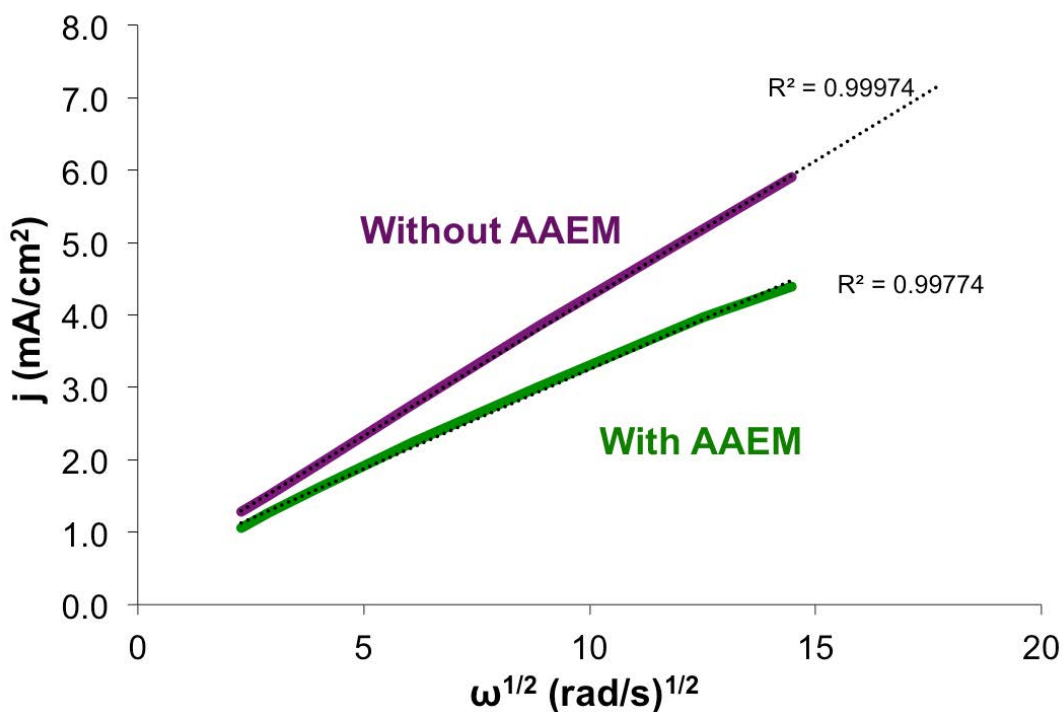


Figure 5. Comparison of Pd₁Cu₁ Levich Equations with and without the AAEM. 1500 rpm in 0.1 M NaOH. $v = 20\text{mV/s}$

5. Conclusions

Under alkaline conditions, pure palladium is clearly the best ORR catalyst we tested with respect to its fast kinetics and reaction pathway. Because of its high cost, we looked at other compositions comprised of palladium and copper while using an alkaline anion exchange membrane. Consistent with previous work from past group members, the Pd₁Cu₁₁ was still the best composition, even with the added AAEM. The electrode had a very good onset potential, comparable to a palladium rich electrode, while significantly reducing the price to about half. When the membrane was added, we observed an interesting shift of the cathodic sweep to a more positive onset potential. However, the membrane seems to have caused the current to decrease, likely due to transport limitations. More experimentation will be required to determine whether the membrane is causing a 2-electron mechanism instead of a 4-electron mechanism, or whether there were problems with the surface of the electrode itself.

6. Acknowledgments

This work made use of the Cornell Center for Materials Research Shared Facilities, which are supported through the NSF MRSEC program (DMR-1120296) and the Cornell Center for Materials Research REU Program, which is supported through the NSF (M091112).

7. References

- (1) Abby Van Wassen's unpublished work
- (2) Noonan, K.J.T.; Hugar, K.M.; Kostalik, H.A.; Lobkovsky, E.B.; Abruña, H.D.; Coates, G.W. *J. Am. Chem. Soc.* 2012, 134 (44), 18161-18164
- (2) Blizanac, B.B.; Ross, P.N.; Markovic, N.M. *Electrochimica Acta* **2007**, 52 (6), 2264-2271.

Using Thermal Gradients to Understand Local Magnetization Dynamics in Nanoscale Bilayer Systems

Irene Zhang¹, Isaiah Gray², Gregory Fuchs²

¹Department of Physics, Columbia University, New York, NY 10027

²Department of Applied and Engineering Physics, Cornell University, Ithaca, NY 14853

Abstract

New magnetothermal microscopy techniques show great promise for imaging magnetic dynamics at the nanoscale. In order to accurately and reliably measure magnetization in materials using magnetothermal microscopy, it is useful to first have a systematic approach to characterizing their thermal properties. In particular, optically thin films and heterostructures present unique challenges to thermal characterization. In this paper, we develop such an approach based on time domain thermoreflectance. Analytic and computational models are presented, as well as the expected signal measured by time domain thermoreflectance measurements on a Pt/CoFeB bilayer. As expected, the signal grows and then decays as the pump and pulse trains overlap and then pass each other with varying delay time. The signal is also periodic with the repetition rate of the lock-in amplifier, as expected.

1 Introduction

In recent years, spintronics has emerged as a promising application of magnetoelectronics. By controlling the spins of electrons in materials through magnetic effects, researchers are able to develop and improve upon technologies such as random access memory, nanoscale microwave sources, and ultra-low power signal transfer.^[1]

To better study the effects that allow for these technologies and to understand the fundamental magnetoelectronics that may give rise to further developments in spintronics, it is necessary to be able to study the magnetic properties of materials at fundamental length scales. A technique for doing so that is currently being developed is microscopy based on magneto-thermal effects. Previous efforts to characterize the magnetization of materials have relied on magneto-optic microscopy, which has limited spatial resolution. This difficulty is a result of diffraction, which sets the upper bound of the resolution of a light-based microscope as a function of its numerical aperture.^[1] Heat-based microscopy would be able to overcome this fundamental limit.

Thus far, magneto-thermal microscopy has been able to study magnetization in materials through two effects, the Time-Resolved Anomalous Nernst Effect (TRANE) and a combination of the Spin Seebeck Ef-

fect (SSE) and the Inverse Spin Hall Effect (ISSE).^{[1][2]} Both these effects relate the magnetization of a material and the thermal gradient created by a pulsed laser to an electric field, which can then be measured as a voltage signal. The electric field is localized, extending as far as the thermal gradient, meaning that resolution is limited only by the size of the gradient. Accurate extraction of magnetization effects from this voltage signal, however, requires the ability to predict the thermal response of the material to the laser. Until now, such thermal characterization has been done on a case-by-case basis and on materials with relatively easy to understand thermal properties, such as metals. The lack of a systematic approach to characterizing the thermal properties of samples hinders our ability to understand more complicated materials and structures, including topological insulators and bilayers, which may not have such simple thermal properties.

A proposed method of developing a standardized approach is through the use of Time Domain Thermoreflectance (TDTR) measurements. TDTR relates the change in reflectivity of a material to its change in temperature. In a typical TDTR experiment, a laser generates a beam which is then split into two trains of ultra-fast pulses, a pump pulse train and a probe pulse train, incident upon a sample. The pump pulse

creates a thermal response in the material, which in turn creates a transient change in reflectance. [3] The probe pulse, after being sent through a delay line, then measures this reflectance change, which can then be turned into a voltage signal. By varying the delay time between the pump and probe pulse trains, TDTR experiments can measure the temporal evolution of the temperature response.

By comparing experimental TDTR results with thermal diffusion models for pulsed laser heating, thermal parameters such as thermal diffusivity and conductivity can be extracted, and the amount of heat and light absorbed by the sample can be measured, which previous experiments have not been consistently able to accomplish. TDTR measurements have been successfully performed and modeled on single layer films and multilayered structures with film thicknesses on the order of 100 nm. However, once film thicknesses reach optically thin levels wherein the thickness of the film is comparable to the skin depth of the material, modeling the thermal response of multilayered structures becomes significantly more challenging, as the assumption of surface heating is no longer valid. In this project, we attempted to develop analytic and computational models for pulsed laser heating of multilayered structures valid for optically thin films for use in determining thermal parameters through TDTR experiments.

2 Methods

An analytic and a computational model were developed based on the Fourier model for heat diffusion assuming a laser heat source that attenuates exponentially with increasing depth into the sample. The time-domain temperature profile of the stack can then be Fourier transformed into frequency space where it is convolved with the probe pulse to create a signal that would be measured by the lock-in amplifier in a TDTR experiment. The reflectivity response is given by [4]

$$\text{Re}[\Delta R(t)] = \frac{dR}{dT} \sum_{m=-M}^M (\Delta T(m/\tau + f) + \Delta T(m/\tau - f)) \exp(2\pi i m t / \tau) \quad (1)$$

$$\text{Im}[\Delta R(t)] = -i \frac{dR}{dT} \sum_{m=-M}^M (\Delta T(m/\tau + f) - \Delta T(m/\tau - f)) \exp(2\pi i m t / \tau) \quad (2)$$

where t is the delay time between pump and probe pulses, $\Delta R(t)$ is the change in reflectivity, $\Delta T(t)$ is

the frequency domain change in temperature, τ is the repetition rate of the laser and f is the frequency of the lock-in amplifier. The derivative with respect to temperature, $\frac{dR}{dT}$, is shown to be approximately constant near room temperature. The real and imaginary components of the calculated reflectivity response, when measured through a fast photodiode, are directly proportional to the in-phase and out-of-phase voltage signals of the lock-in amplifier. The procedure described above is completed in full for a Pt/CoFeB bilayer with a sapphire using the computational model. A sample calculation of $\frac{dR}{dT}$ based on the Wiedemann-Franz Law is also done for the CoFeB bilayer.

2.1 Analytic model

Because the thermal gradient in the sample dissipates before it spreads far laterally, the heat diffusion through the sample is treated as a one dimensional problem. We start with the one-dimensional heat equation with a source term that decays exponentially in the z -direction,

$$D_1 \frac{\partial^2 T}{\partial z^2} + \frac{\partial T}{\partial t} = q_1 e^{-\alpha_1 z} \quad (3)$$

where D_1 is the thermal diffusivity, q_1 is the initial power absorbed at the interface, and α_1 is the absorption coefficient. Since we expect the temperature response to be periodic in time, we consider only a single mode and assume the solution is separable. A similar method for modeling heat diffusion through multilayered structures for periodic point sources has been described by Feldman. [5] For the general case, we can compute the Fourier series expansion of the time-dependent boundary conditions and solve for each mode using its respective Fourier coefficient as the boundary condition of the differential equation to be discussed. With the assumption that $T(z, t) = T(t)Z(z) = e^{i\omega t} Z(z)$, the equation becomes an ordinary differential equation,

$$\frac{\partial^2 Z}{\partial z^2} T(t) + \frac{i\omega}{D_1} T(t) = \frac{q_1}{D_1} e^{-\alpha_1 z}. \quad (4)$$

The general solution for the homogeneous equation can be written, following Feldman's notation,

$$Z(z) = T^+ e^{iu_1 z} + T^- e^{-iu_1 z} \quad (5)$$

where $u_1 = \sqrt{\frac{i\omega}{D_1}}$. A particular solution can be written $T_p = B e^{-\alpha_1 z}$, and substituting into the ODE gives $B = \frac{q_1/D_1}{\frac{i\omega}{D_1} + \alpha_1^2}$. The general solution for $Z(z)$ is then

$$Z(z) = T^+ e^{iu_1 z} + T^- e^{-iu_1 z} + \frac{q_1/D_1}{u_1^2 + \alpha_1^2} e^{-\alpha_1 z} \quad (6)$$

and

$$T_0 \equiv Z(0) = T^+ + T^- + \frac{q_1/D_1}{u_1^2 + \alpha_1^2} \quad (7)$$

We then define the flux $F \equiv -k_1 \frac{dZ}{dz}$, where k_1 is the thermal conductivity, and evaluate the flux at the boundary $F_0 \equiv F(0)$:

$$F(z) = -k_1 (T^+ iu_1 e^{iu_1 z} - T^- iu_1 e^{-iu_1 z} - \frac{q_1 \alpha_1 / D_1}{u_1^2 + \alpha_1^2} e^{-\alpha_1 z}) \quad (8)$$

$$F_0 = -k_1 \left(T^+ iu_1 - T^- iu_1 - \frac{q_1 \alpha_1 / D_1}{u_1^2 + \alpha_1^2} \right). \quad (9)$$

Solving equations 7 and 9 for T^+ and T^- , we obtain

$$T^+ = \frac{1}{2} T_0 - \frac{1}{2k_1 iu_1} f_0 - \frac{q_1 \alpha_1 / D_1}{u_1^2 + \alpha_1^2} \left(\frac{1}{2} - \frac{\alpha_1}{2iu_1} \right) \quad (10)$$

$$T^- = \frac{1}{2} T_0 + \frac{1}{2k_1 iu_1} f_0 - \frac{q_1 \alpha_1 / D_1}{u_1^2 + \alpha_1^2} \left(\frac{1}{2} + \frac{\alpha_1}{2iu_1} \right) \quad (11)$$

giving

$$\begin{aligned} Z(z) = & \frac{1}{2} T_0 - \frac{1}{2k_1 iu_1} f_0 - \frac{q_1 \alpha_1 / D_1}{u_1^2 + \alpha_1^2} \left(\frac{1}{2} - \frac{\alpha_1}{2iu_1} \right) e^{iu_1 z} \\ & + \frac{1}{2} T_0 + \frac{1}{2k_1 iu_1} f_0 - \frac{q_1 \alpha_1 / D_1}{u_1^2 + \alpha_1^2} \left(\frac{1}{2} + \frac{\alpha_1}{2iu_1} \right) e^{-iu_1 z} \\ & + \frac{q_1 / D_1}{u_1^2 + \alpha_1^2} e^{-\alpha_1 z} \quad (12) \end{aligned}$$

This expression gives the temperature at depth z in a semi-infinite material given the boundary temperature and flux, T_0 and F_0 . To extend to a multilayered structure, we solve the analogue to equation 4 in each layer and use the temperature and flux evaluated at the end of the previous layer as the initial temperature and flux of the current layer. Let L_n and z_n be the thickness and location of the lower boundary of the n th layer, respectively. Evaluating $Z_1 \equiv Z(z_1)$ and $F_1 \equiv F(z_1)$ and reexpressing complex exponentials in polar form, we find

$$\begin{aligned} Z_1 = & T_0 \cos u_1 z_1 - \frac{F_0}{k_1 u_1} \sin u_1 z_1 \\ & - \frac{q_1 / D_1}{u_1^2 + \alpha_1^2} \left(\frac{\alpha_1}{u_1} \sin u_1 z_1 - \cos u_1 z_1 + e^{-\alpha_1 z_1} \right) \quad (13) \end{aligned}$$

$$\begin{aligned} F_1 = & T_0 k_1 u_1 \sin u_1 z_1 - F_0 \cos u_1 z_1 - \frac{q_1 k_1 / D_1}{u_1^2 + \alpha_1^2} \\ & \times (u_1 \sin u_1 z_1 + \alpha_1 \cos u_1 z_1 - \alpha_1 e^{-\alpha_1 z_1}), \quad (14) \end{aligned}$$

which can then be expressed in matrix form

$$\begin{bmatrix} T_1 \\ F_1 \end{bmatrix} = A_1 \begin{bmatrix} T_0 \\ F_0 \end{bmatrix} + Q_0 \quad (15)$$

$$A_1 = \begin{bmatrix} \cos u_1 z_1 & -\frac{1}{k_1 u_1} \sin u_1 z_1 \\ k_1 u_1 \sin u_1 z_1 & \cos u_1 z_1 \end{bmatrix} \quad (16)$$

$$Q_0 = \frac{q_1 / D_1}{u_1^2 + \alpha_1^2} \begin{bmatrix} \frac{\alpha_1}{u_1} \sin u_1 z_1 - \cos u_1 z_1 + e^{-\alpha_1 z_1} \\ -k_1 (u_1 \sin u_1 z_1 + \alpha_1 \cos u_1 z_1 - \alpha_1 e^{-\alpha_1 z_1}) \end{bmatrix} \quad (17)$$

For the second layer, the analogous ODE is

$$\frac{\partial^2 Z}{\partial \xi^2} + \frac{i\omega}{D_2} Z = q_2 e^{-\alpha_2 \xi} \quad (18)$$

where $\xi = z - z_1$ and $q_2 = q_1 e^{-\alpha_1 z_1}$, and α_2 and D_2 are the absorption coefficient and thermal diffusivity, respectively, of material 2. Since this equation is identical to equation 4 barring different parameters we can write out the expressions for the temperature and flux at boundary 2

$$\begin{bmatrix} T_2 \\ F_2 \end{bmatrix} = A_2 \begin{bmatrix} T_1 \\ F_1 \end{bmatrix} + Q_1 \quad (19)$$

$$A_2 = \begin{bmatrix} \cos u_2 L_2 & -\frac{1}{k_2 u_2} \sin u_2 L_2 \\ k_2 u_2 \sin u_2 L_2 & \cos u_2 L_2 \end{bmatrix} \quad (20)$$

$$Q_2 = \frac{q_2 / D_2}{u_2^2 + \alpha_2^2} \begin{bmatrix} \frac{\alpha_2}{u_2} \sin u_2 L_2 - \cos u_2 L_2 + e^{-\alpha_2 L_2} \\ -k_2 (u_2 \sin u_2 L_2 + \alpha_2 \cos u_2 L_2 - \alpha_2 e^{-\alpha_2 L_2}) \end{bmatrix} \quad (21)$$

which can then be expressed in terms of T_0 and F_0

$$\begin{bmatrix} T_2 \\ F_2 \end{bmatrix} = A_2 A_1 \begin{bmatrix} T_0 \\ F_0 \end{bmatrix} + A_2 Q_1 + Q_0 \quad (22)$$

This process can be iterated for n layers, giving a 2×2 system in which specifying two out of T_0 , F_0 , T_n , and F_n allows one to determine the other two. The temperature within each layer is given by equation 6 with the appropriate parameters substituted.

2.2 Computational model

Finite element analysis was completed using the COMSOL simulation package. The heat transfer module was used to model the temperature response of a $5 \mu\text{m}$ by $15 \mu\text{m}$ Pt/CoFeB/Al₂O₃ stack to a 3 ps laser pulse at normal incidence. The Pt/CoFeB/Al₂O₃ sample was modeled as a $5 \mu\text{m}$ by $15 \mu\text{m}$ by $0.1 \mu\text{m}$ block with three layers of thicknesses 4 nm, 4 nm, and 92 nm, respectively. Values for the thermal conductivity, heat capacity, and density for each material were taken

Material	Thermal conductivity (W m ⁻¹ K ⁻¹)	C _p (J K ⁻¹ mol ⁻¹)	Density (kg m ⁻³)
Pt	20 ^[6]	133 ^[7]	21500 ^[7]
CoFeB	87 ^[8]	440 ^[8]	8000 ^[8]
Al ₂ O ₃	23.1 ^[9]	761 ^[10]	3980 ^[11]

Table 1: Thermal and mechanical properties used for each layer of the COMSOL geometry.

from the literature and, where possible, values specific to optically thin films were used (see Table 1).

The laser was modeled as a heat source incident on a spot of radius 2 μm with the form

$$Q_{in} = Q_0(1 - R_c)A_c \frac{1}{\pi\sigma_x\sigma_y} e^{-\frac{x^2}{2\sigma_x^2} - \frac{y^2}{2\sigma_y^2}} e^{-A_c|z|} \times e^{-\left(\frac{t}{\text{pulse.width}}\right)^2} \quad (23)$$

with values used for each parameter given in Table 2.

Order of magnitude estimates were made for the interfacial thermal resistances at the Pt/CoFeB and CoFeB/Al₂O₃ interfaces based on literature values for metal-metal and metal-dielectric interfaces^{[14][15]} since no measurements of interfacial thermal resistance have been made for these interfaces. The simulation was run for 100 ns, with a time step of 5 ps for times up to 0.1 ns and an increased time step of 0.1 ns for times after to lower the computation time. Although the full three dimensional temporal temperature profile was simulated, only the temperature and time data along the z- axis were exported for processing. The z-axis time domain temperature data were transformed into frequency space using a Fast Fourier Transform (FFT), and an interpolated function was created to evaluate ΔT in equations 1 and 2.

2.3 Calculation of $\frac{dR}{dT}$

A sample calculation for the temperature dependence of reflectance was done for the sample in the above section. Previous work from Y. Laaziz et al^[14] shows that the reflectance of an a film-substrate sample is given by

$$R = R_f + \frac{T_f^2 R_3}{1 - R_3 R'_f} \quad (24)$$

where R_f is the front-end reflectance, T_f the transmittance, and R'_f is the back reflectance. These quantities

can in turn be expressed in terms of the reflectances of each interface:

$$T_f = \frac{(1 - R_1)(1 - R_2)}{e^{\alpha d} + R_1 R_2 e^{-\alpha d} + 2\sqrt{R_1 R_2} \cos(\delta_1 + \delta_2 - \phi)} \quad (25)$$

$$R_f = \frac{R_1 e^{\alpha d} + R_2 e^{-\alpha d} + 2\sqrt{R_1 R_2} \cos(\delta_1 - \delta_2 + \phi)}{e^{\alpha d} + R_1 R_2 e^{-\alpha d} + 2\sqrt{R_1 R_2} \cos(\delta_1 + \delta_2 - \phi)} \quad (26)$$

$$R'_f = \frac{R_2 e^{\alpha d} + R_1 e^{-\alpha d} + 2\sqrt{R_1 R_2} \cos(\delta_2 - \delta_1 + \phi)}{e^{\alpha d} + R_1 R_2 e^{-\alpha d} + 2\sqrt{R_1 R_2} \cos(\delta_1 + \delta_2 - \phi)} \quad (27)$$

Here R_1 , R_2 , and R_3 are the reflectances of the (1) air-film, (2) film-substrate, and (3) substrate-air boundaries, respectively; δ_1 and δ_2 are the phases of the Fresnel coefficients of boundaries (1) and (2); α is the extinction coefficient in the film; and ϕ is the change in optical path length of the light after twice crossing the film.

Classically, the above quantities can be expressed in terms of the real and imaginary parts of the complex index of refraction^[15]

$$\tilde{N} = \sqrt{\varepsilon\mu \left(1 + \frac{4\pi i\sigma}{\varepsilon\omega}\right)} = \tilde{n} + i\tilde{k} \quad (28)$$

$$R = \frac{(\tilde{n}_1 - \tilde{n}_2)^2 + \tilde{k}_2^2}{(\tilde{n}_1 + \tilde{n}_2)^2 + \tilde{k}_2^2} \quad (29)$$

$$\delta = \arctan \frac{-2\tilde{k}}{10\tilde{n}^2 - \tilde{k}^2} \quad (30)$$

$$\alpha = \frac{4\pi\tilde{k}}{\lambda} \quad (31)$$

$$\phi = \frac{4\pi\tilde{n}d}{\lambda} \quad (32)$$

where ε is the absolute permittivity of the materia, μ is the magnetic permeability (taken to be 1), and ω is the frequency of the laser. The optical conductivity is related to the temperature through the Wiedemann-Franz law^[16]:

$$\sigma = \frac{\kappa}{LT} \quad (33)$$

Variable	Parameter	Value
Q_0	Total laser power	26 W
R_c	Reflection coefficient	0.2 ^[12]
A_c	Absorption coefficient	$7.84 \times 10^5 \text{ cm}^{-1}$ ^[13]
<i>pulse_width</i>	Temporal pulse width	3 ps
σ_x	x standard deviation	2 μm
σ_y	y standard deviation	2 μm

Table 2: Parameters used to define the heat source of the heat transfer module and their values.

where κ is the thermal conductivity and L is the Lorenz number which is given by $L = \frac{\pi^2}{3} \left(\frac{k_B}{e}\right)^2$. The Weidemann-Franz law is valid for metals at and above room temperature, but for insulators a more sophisticated approach is needed. For the Pt/CoFeB bilayer, ε and κ were averaged over the thickness of the two layers. The reflectance was then calculated as a function of temperature and the derivative taken at $T = 300 \text{ K}$. The effects of varying thermal conductivity κ and layer thickness d were also studied.

3 Results

3.1 COMSOL simulation

The temporal evolution of the simulated pulsed heating of a Pt/CoFeB bilayer shows a rapid rise and then slower decay in both layers. Along the z -axis, the temperature profile remains surprisingly continuous, with no large jumps at the interfaces between layers (Figure 1). Although the interfacial thermal resistances were entered into the COMSOL model, they do not seem to have significantly hindered heat flow between the layers. In the case of the Pt/CoFeB interface, we suspect this is because the interfacial thermal resistance at metal-metal interfaces should be low due to metals having similar thermal transport mechanisms and high optical and thermal conductivities. In the case of the CoFeB/ Al_2O_3 interface, the heat has largely dissipated by the time it reaches the end of the CoFeB layer that any transfer to the substrate would be negligible anyway.

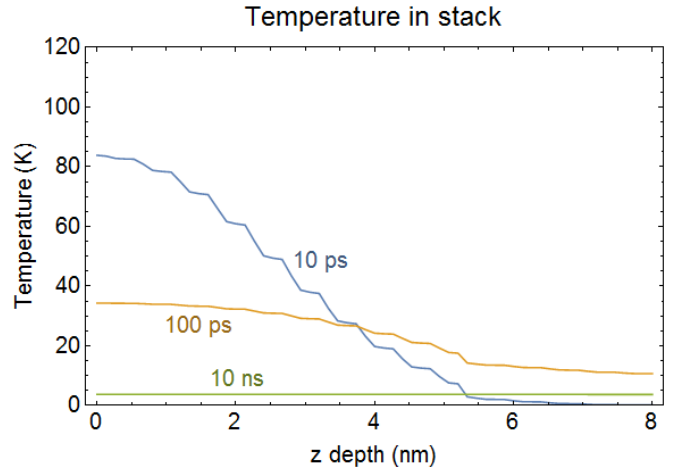


Figure 1: COMSOL temperature data plotted against depth at $t = 10 \text{ ps}$, 100 ps and 10 ns . Step effects are due to finite element size.

3.2 $\frac{dR}{dT}$ calculation and sensitivity

After taking the FFT of the temporal profile, the frequency space temperature response was evaluated at the frequency of the lock-in amplifier (10 kHz) offset by integral multiples of the laser repetition rate (76 MHz), and was then convolved with the probe pulse train (assumed to be a delta function) (equations 1 and 2). The expected temperature dependence of the reflectance of the Pt/CoFeB bilayer was then evaluated near room temperature (Figure 2). $R(T)$ can be approximated to be linear in this regime, and $\frac{dR}{dT}$ was calculated to be $2.042 \times 10^{-4} \text{ K}^{-1}$.

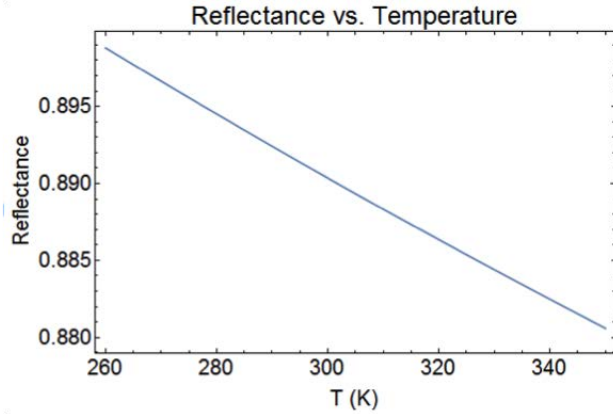


Figure 2: Reflectance of the Pt/CoFeB bilayer plotted as a function of temperature for $T = 260$ K to 360 K. The function is approximately constant with a slope of $2.042 \times 10^{-4} \text{ K}^{-1}$.

The sensitivity of the reflectance at room temperature to thermal conductivity and layer thickness are shown in Figures 3 and 4. The calculated reflectance is extremely sensitive to changes in thermal conductivity in the range between 0 and $2 \times 10^5 \text{ W K}^{-1} \text{ m}^{-1}$ and less so beyond this range. The dependence of the calculated reflectance on layer thickness, on the other hand, largely disappears after 10 nm but highly sensitive for very thin films. This suggests that for room temperature experiments, $\frac{dR}{dT}$ should remain stable for thicker films and for materials with high thermal conductivity, such as metals.

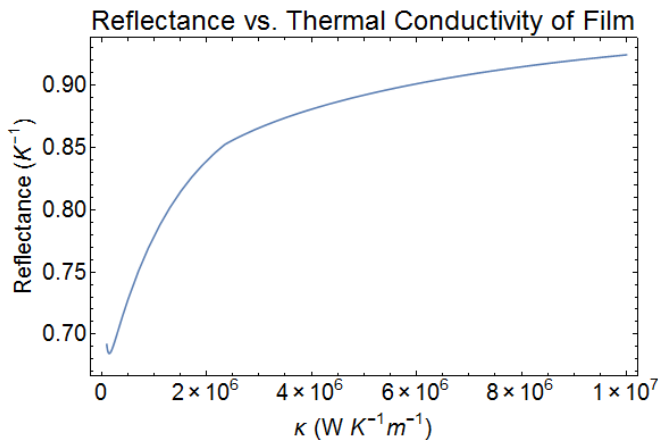


Figure 3: Reflectivity plotted against thermal conductivity at $T = 300$ K. All other parameters are held fixed at their values for the Pt/CoFeB bilayer.

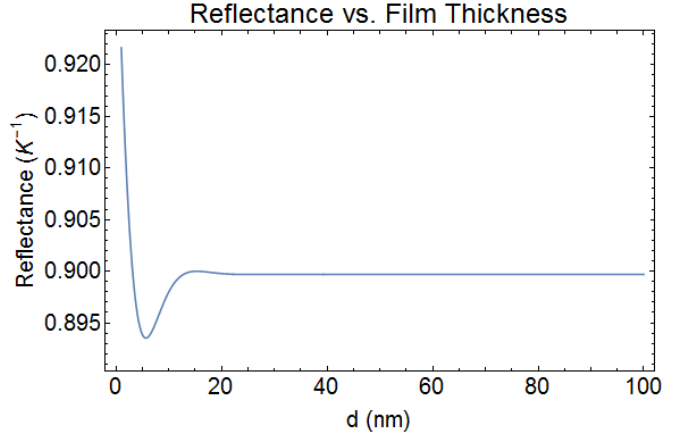


Figure 4: Reflectivity plotted against film thickness at $T = 300$ K. All other parameters are held fixed at their values for the Pt/CoFeB bilayer.

3.3 Expected change in reflectance

The total change in reflectance, given by equation 1, for the Pt/CoFeB/ Al_2O_3 system is shown to be periodic with respect to delay time. As the delay time is varied, the pump and pulse trains overlap, creating a larger signal, and then pass beyond each other, resulting in a weakened signal. Once the delay reaches the period of the laser, the signal should return to its initial value. The differences in peak heights shown in Figure 5 are possibly due to the sampling rate of the computational analysis.

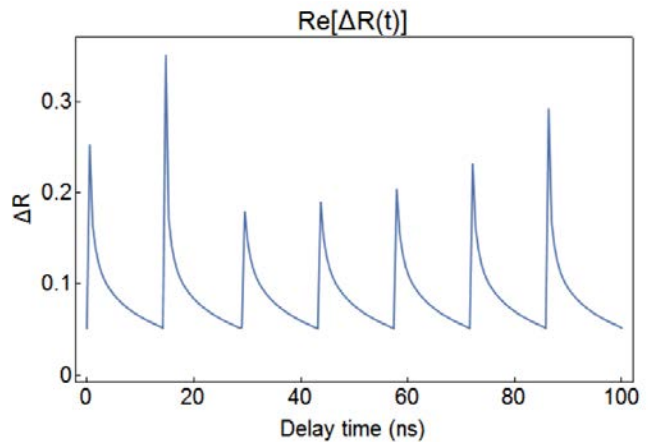


Figure 5: Real part of the expected change in reflectance computed as a function of delay time for the Pt/CoFeB bilayer. As expected, the signal has a period of about 13 ns.

4 Conclusion

Two models, one analytic and one computational, for pulsed laser heating of optically thin multilayered films were presented in this paper. The analytic model solves the heat diffusion equation for a single mode of a periodic source and extends this solution to multiple layers using an iterated matrix method. The computational model makes use of finite element analysis to calculate the expected frequency space temperature response, which is then used to determine the expected reflectance signal. Further work can be done to improve the current model by extending the treatment of $\frac{dR}{dT}$ beyond the limits of the Wiedemann-Franz model. By comparing this signal to TDTR experimental data, we hope to be able to systematically extract the thermal parameters of materials. Further TDTR experiments would also better determine the validity of applying the Fourier model of heating to these types of structures.

5 Acknowledgements

Many thanks to Professor Greg Fuchs for providing such an interesting project, Isaiah Gray for his mentorship and guidance, and all the members of the Fuchs lab for their help and support. This work was supported by the Cornell Center for Materials Research with funding from the NSF MRSEC program (DMR-1120296) and the REU Site program (DMR-1063059).

6 References

1. J.M. Bartell, D. H. Ngai, Z. Leng, and G. D. Fuchs. Toward a table-top microscope for nanoscale magnetic imaging using picosecond thermal gradients. *Nat. Commun.* 6, 8460 (2015).
2. F. Guo, J. M. Bartell, and G. D. Fuchs. Ferromagnetic resonance phase imaging in spin Hall multilayers *Phys. Rev. B* 93, 144415 (2016).
3. K. Kang, Y.K. Koh, C. Chiritescu, X. Zheng, D.G. Cahill. Two-tint pump-probe measurements using a femtosecond laser oscillator and sharp-edged optical filters. *Review of Scientific Instruments* 79, 114901 (2008).
4. D. Cahill. Analysis of heat flow in layered structures for time-domain thermoreflectance.” *Review of Scientific Instruments.* 75, 5119 (2003).
5. A. Feldman, *High Temp. - High Press.* 31, 293 (1999).
6. S. Yoneoka, J. Lee, M. Liger, G. Yama, T. Kodama, M. Gunji, J. Provine, R. T. Howe, K.E. Goodson, T. W. Kenny. Electrical and Thermal Conduction in Atomic Layer Deposition Nanobridges Down to 7 nm Thickness. *Nano Lett.* 12, 683 686 (2012).
7. D. R. Lide (ed). *CRC Handbook of Chemistry and Physics*, 84th Edition. (CRC Press, Boca Raton, 2003).
8. F. Busse, M. Mansurova, B. Lenk, M. von der Ehe, and M. Mnzenberg. A scenario for magnonic spin-wave traps. *Scientific Reports* 5, 12824 (2015)
9. Y.S. Touloukian, S. C. Saxena, and P. Hestermans. *Thermophysical Properties of Matter*, vol. 2. (IFI/Plenum, New York, 1970).
10. D. A. Ditmars, S. Ishihara, S. S. Chang, and G. Bernstein. Enthalpy and Heat-Capacity Standard Reference Material: Synthetic Sapphire (a-A1203) from 10 to 2250 K. *J. Res. Nat. Bur. Stand.* 87 (2), 159-163 (1982).
11. E. Dobrovinskaya, L. A. Lytvynov, and V. Pishchik. *Sapphire: Material, Manufacturing, Applications.* (Springer US, New York, 2009).
12. O. S. Heavens. *Optical Properties of Thin Solid Films.* (Dover, New York, 1991).
13. A. D. Raki, A. B. Djurii, J. M. Elazar, and M. L. Majewski. Optical properties of metallic films for vertical-cavity optoelectronic devices. *Appl. Opt.* 37, 5271-5283 (1998)
14. B. C. Grundum, D. G. Cahill, R. S. Averback. Thermal conductance of metal-metal interfaces. *Phys Rev B.* 72, 245426 (2005)
15. H. Lyeo, D. G. Cahill. Thermal conductance of interfaces between highly dissimilar materials. *Phys. Rev. B.* 73, 144301 (2006)
16. Y. Laaziza, A. Bennounaa, N. Chahbouna, A. Outzourhita, E.L. Ameziane. Optical characterization of low optical thickness thin films from transmittance and back reflectance measurements. *Thin Solid Films* 372, 149155 (2000)
17. M. S. Dresselhaus, *Solid State Physics Part 11, Opt. Prop. Solids.* lecture notes (2001).
18. W. Jones, N. H. March. *Theoretical Solid State Physics.* (Dover, New York, 1985)

Fabrication of piezo scanners for MRI-compatible multiphoton microscope

Vesta Zhelyaskova¹, Najva Akbari², Chris Xu²

¹Department of Physics, University of Florida, Gainesville, FL, 32611

²School of Applied and Engineering Physics, Cornell University, Ithaca, NY, 14853

Background

MRI and MPM

Nuclear magnetic resonance imaging (MRI) and X-ray computed tomography (CT) are the most common brain imaging methods. MRI (as well as other similar imaging methods such as fMRI, DTI, etc.) provide insights into the structure and function of the brain, unachievable by other imaging methods such as CT. Based on the tendency for nuclei of nonzero spin to resonate while irradiated by oscillating magnetic fields of a specific frequency, MRI machines collect information about the tissue types, abundance, and location in the body. MRI, however, limits us to macroscopic imaging. In order to more closely follow the evolution and mechanisms of brain functions, a microscopic, cellular view is necessary.

Multiphoton microscopy (MPM) images the fluorescence of molecules with cellular resolution. One-photon fluorescence is not compatible with brain imaging because of the signal attenuation resulting from the scattering of light by body tissues. Multiphoton fluorescence, however, can use a light source with a wavelength longer than the one required for one-photon excitation. Longer wavelengths of light more easily penetrate barriers, such as the skull. MPM uses the concept of multiphoton absorption/fluorescence. Instead of irradiating the cells with high-energy radiation, the cells can be irradiated more intensely with low-energy radiation (with a wavelength approximately twice or three times that of the one required for excitation). Therefore, molecules fluoresce upon simultaneously absorbing multiple photons of lower energy. The probability of the simultaneous absorption of multiple photons is much lower than that of the absorption of just one. Thus, a higher intensity (photon density) is necessary. This can be achieved by using laser pulses on the order of femtoseconds. The use of a pulsed laser lowers the average power and decreases the risk of thermal damage to the cells. The high intensity of laser irradiation changes the linear relationship of signal strength and light intensity. For two-photon fluorescence, the signal strength becomes proportional to the square of the intensity of the laser light. Multiphoton electron transitions occur, with higher probability, at the laser focal point. Farther from the focus, the intensity of the laser is too weak to stimulate a collectable fluorescence. For this reason, multiphoton microscopy also has the advantage of an improved signal and decreased background noise.

Second harmonic generation (SHG), the signal of two-photon excitation, is more often monitored than third harmonic generation (THG). THG, however, can resolve cellular structures almost twice as deep in the brain. Three photon microscopy (3PM) has been shown to penetrate up to 2.5 mm through the skull.¹

COMPMRI System

Professor Chris Xu and his lab group have proposed combining the two technologies, MPM and MRI, into a concurrent multiphoton magnetic resonance imaging (COMPMRI) system (Fig. 1). The system will allow researchers to simultaneously image the brain using MRI and nonlinear optical imaging techniques. As the MR signals are collected, the MRI-compatible three photon microscope scans multiple regions of the brain. The MRI machine will slowly, macroscopically image the brain. At the same time, the MPM images with cellular resolution revealing the details in anatomical structures and brain function that are not accessible with MRI.

The COMPMRI system consists of a pulsed laser (1.2 μm to 1.9 μm), a piezoelectric scanner, coupled fibers, an objective lens, and an RF coil array. The laser light is coupled into the fibers, which are resting on the piezo scanner. The scanner, composed of two bimorphs, drives the fibers at their resonant frequency. Using mirrors, the light delivered by the fibers is directed into the objective to raster-scan a plane of the brain area under investigation. The fluorescence signal or the harmonic generation is collected and amplified with photomultiplier tubes. The image is then generated as a map of signal intensity as a function of beam position. Axial shifting changes the focal point of the light source and a series of 2D “slices” can be imaged for a 3D reconstruction of the brain region.

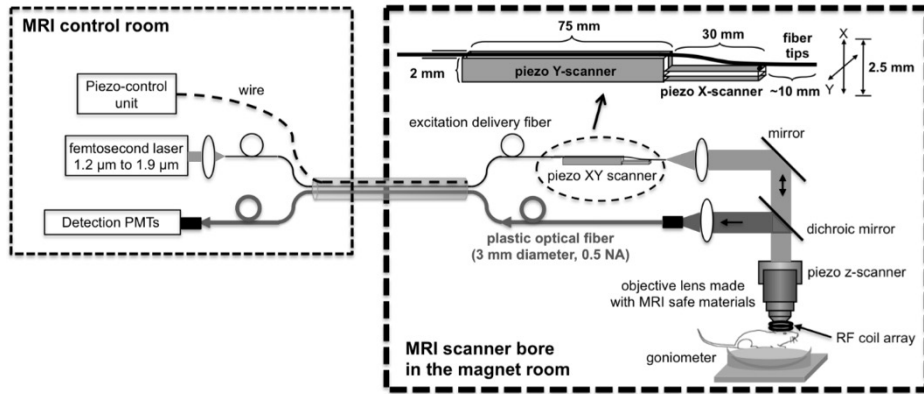


Fig. 1. COMPMRI system setup.

Theory/Modeling

The design of the piezo scanner is based on one used in a MPM endoscope.² Two piezoelectric bimorphs are attached perpendicularly as shown in Fig. 2. The two piezoceramic materials composing each bimorph are oppositely poled. With a voltage of 200 Vpp applied to the bimorph, the piezoceramics bend. The larger, “slow” bimorph is driven at a frequency of approximately 4 Hz. The smaller, “fast” bimorph is driven at the resonant frequency of the attached fibers, approximately 1 kHz. When both bimorphs are driven simultaneously, a rectangular area is raster-scanned by the fibers.

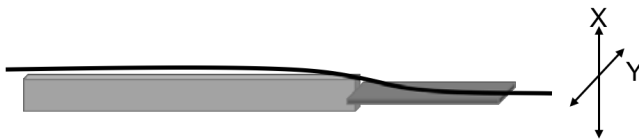


Fig. 2. Sketch of the constructed piezo scanner. The longer, slow axis bimorph deflects the optical fibers in the Y-direction. The shorter, fast axis bimorph deflects the fibers in the X-direction. Together, the

By modeling the slow axis as an arc and the fast axis and fiber combination as a linear extension, the deflection of the fibers can be calculated. Assuming the bimorphs bend at small angles, the total deflection can be expressed as

$$D = 2c(L_1^2 + 2L_1L_2) \times \left(\frac{V_{\text{applied}}}{V_{\text{specification}}} \right) \quad (1)$$

where L_1 is the free length of the non-resonant bimorph; L_2 is the sum of the length of the resonant bimorph and the overhang length of the fiber; c is a proportionality constant dependent on initial parameters set by bimorph manufacturers ($c = 1.83 \times 10^{-4} \text{ mm}^{-1}$); and $V_{\text{specification}}$ is provided by the bimorph manufacturers.³

The lengths of our bimorphs were selected based on a desired deflection of at least 2.5 mm. Previously, bimorphs in this set up have shown to achieve a deflection of only 95% of the the calculated value. Taking this loss into considerations, calculations were made using a total deflection value of 2.625 mm. Two piezo scanners were built with two unique combinations of active piezo bimorph lengths: (A) slow bimorph length = 30 mm, fast bimorph length = 6 mm; (B) slow bimorph length = 35 mm, fast bimorph length = 20 mm. Each bimorph as a width of 1.5 mm and a thickness of 0.38 mm.

Ideally, the fibers should have a resonant frequency on the order of 1 kHz. The free hanging length required to achieve resonance can be calculated using

$$v = \frac{\beta R}{4\pi L^2} \sqrt{\frac{E}{\rho}} \quad (2)$$

where R is the radius of the fiber; L is the overhanging fiber length; β is a boundary condition for zeroth-order vibrational mode of a fixed-free cantilever ($\beta \approx 3.52$); ρ is the density (of silica); and E is Young's modulus (for silica). The necessary fiber overhang length is calculated to be 9 mm.³

Eddy Currents Modeling

When placed in the magnetic field of an MRI machine (assumed to have a strength of 3 T), the two thin nickel electrodes on the bimorphs could potentially generate eddy currents disrupting the operating motion of the scanner. The largest eddy currents can be avoided with an advantageous orientation within the bore of the MRI. Minimizing the change in flux through the bimorphs as they bend is crucial.

Resistive eddy currents will be induced even with this advantageous orientation. Calculations of the potential eddy currents and the power dissipated across the electrodes are based primarily on Siakavellas' IEEE 1997 publication on calculating eddy currents on thin conducting plates.⁴ The Improved Model assumes that currents take the paths of minimum energy dissipation. Current paths follow the perimeter of the electrode, but are elliptical in shape. Both of Siakavellas' expressions were modified for the condition of a temporally and spatially uniform magnetic field and a changing electrode area.

$$I(t) = \frac{1}{8\sqrt{\pi}} \frac{\sqrt{\gamma_e}}{1.5(\gamma_e + 1) - \sqrt{\gamma_e}} \frac{(\gamma + 1)\sqrt{\gamma}}{\gamma^2 + 1} \sigma h l a B \omega \theta_0^2 \sin^2(\omega t) \quad (3)$$

$$P(t) = \frac{1}{32\sqrt{\pi}} \frac{\sqrt{\gamma_e}}{1.5(\gamma_e + 1) - \sqrt{\gamma_e}} \frac{(\gamma + 1)\sqrt{\gamma}}{\gamma^2 + 1} \sigma h l^2 a^2 B^2 \omega^2 \theta_0^4 \sin^4(\omega t) \quad (4)$$

σ is the conductivity of the metal; h is the thickness; l and a are the electrode's dimensions; B is the external magnetic field; ω is the frequency of the bimorph; γ is the length to width ratio ($\gamma = \frac{l}{a}$); and γ_e is the ratio of semi-axis of ellipsoidal current paths ($\gamma_e \approx \gamma \frac{\sqrt{\pi}}{2}$); and θ_0 is the approximate maximum angular displacement of the bimorph in radians ($5^\circ = 0.1745 \text{ rad}$).

Calculations of the eddy currents generated in the two piezo scanners are discussed further in the Results and Discussion section.

Fabrication

The bimorphs used in the scanners (T215-A4CL, Piezo Systems, Inc.) were cut to the desired lengths using a Beuhler Isomet Low Speed Diamond Saw. All the pieces were given extra length for their respective attachments. Both of the fast bimorphs have an extra 3 mm with which to attach to the slow bimorphs. Scanner A and B's slow bimorphs have extra lengths of 8 and 5 mm respectively to place into the scanner mount. The extra lengths are made inactive through an etching process. Using a razorblade, the nickel electrodes on both sides of the bimorphs are interrupted width-wise at the desired length. The extra lengths now become inactive and will play no role in the motion of the scanner.

Stripped wires are then soldered onto both sides of the slow bimorphs and onto one side of each of the fast bimorphs. Before soldering wires to the other side of the fast bimorphs, the optical fibers are attached. Two fibers, stripped of their casings at one end, are glued together at the stripped ends. Only one fiber will be coupled into the laser, however. Another is necessary to break the cylindrical symmetry of the first. This process ensures the correct scanning pattern. Using an inspection microscope with an attached camera, the paired fibers are centered and glued, using a UV optical adhesive, onto the soldered side of the fast axis. After curing, the other side of the fast axis is soldered with wires. The inspection microscope, with the help of a mirror for a side view, is used to align both the slow axis into the scanner mount and the fast axis onto the slow axis. Both processes require a 24-hour adhesive-curing time.

The wires attached to the bimorphs and four additional wires (one for each side of each bimorph) are soldered onto the scanner base. Using a frequency generator and an amplifier, a voltage can now be applied across either pair of electrodes. The inspection microscope's CCD camera is used to observe the deflection of the fibers from the motion of the bimorphs. The two perpendicular amplitudes of the fiber's oscillations are recorded by driving each bimorph individually.

Results and Discussion

Eddy Current Calculations

Using equations (3) and (4), the potential generated eddy currents and the total dissipated power across both electrodes of each bimorph were calculated respectively. Two orientations were considered: (a) the scanner's major axis is aligned parallel to the magnetic field and (b) the scanner's major axis is oriented perpendicular to the magnetic field with the non-resonant bimorph's normal area vector parallel to the field lines. The second orientation (b) is shown to be the more favorable of the two, generating smaller currents and dissipating less power. In this set up, the area vector of the resonant bimorph will remain perpendicular to the B field lines so the change in flux as it oscillates is negligible. However, a change of flux is expected as the non-resonant bimorph scans. The generated eddy currents across each of the two slow bimorph electrodes are predicted to be 3.49 mA and 3.54 mA for scanners A and B respectively. The total dissipated power across both non-resonant electrodes is expected to be 0.641 μ W and 0.557 μ W for scanners A and B respectively. Compared to the power applied to the scanners the calculated dissipated power is negligible. The motion of the scanner will therefore be disrupted only negligibly by induced eddy currents.

Deflection

The total deflections of the non-resonant bimorphs were calculated using equation (1). The set up of scanners A and B were expected to yield 1.99 mm and 1.10 mm deflections respectively. Upon testing, the measured deflections were 1.44 mm and 1.38 mm respectively (Fig. 3). Bimorph underperformance is expected. The decrease in deflection could be the result of minor damages to the bimorph sustained during the fabrication of the scanner. Scanner B's measured deflection, however, was greater than expected. This indicates an incorrect modeling of the system. For future calculations, the flexible fibers will not be considered linear extensions; their greater flexibility relative to that of the bimorphs may result in additional deflection. Additionally, Figure 3 shows that for both scanners the deflection is asymmetrical with respect to the initial position. The uneven deflection stems from small differences in the active length after the etching process. The piezoceramic with a larger active length will deflect more.

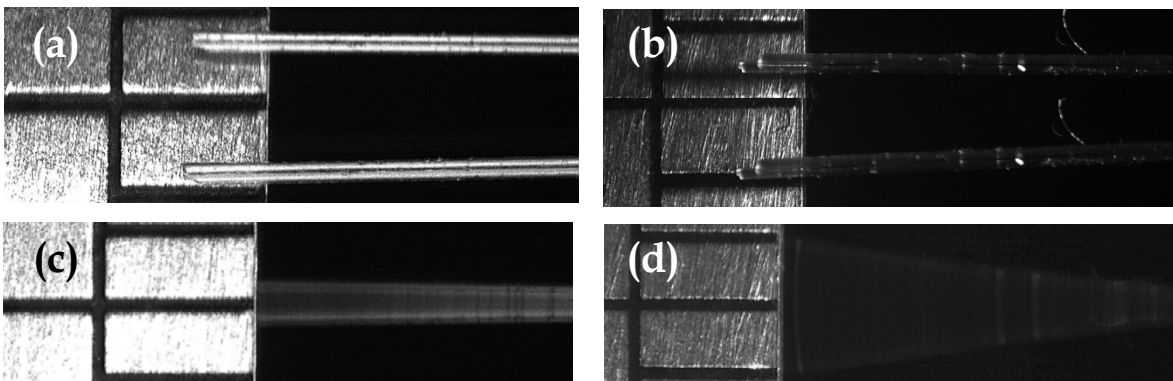


Fig. 3. Images of fiber deflection taken with the CCD camera of an inspection microscope. (a) and (b) show the deflections of fibers from the slow bimorph motion of scanner A and scanner B respectively. (c) and (d) show the deflections of the fibers oscillating at their resonant frequencies, driven by the motion of the fast axis bimorphs of scanners A and B respectively.

Fiber Resonance

Using equation (2), Rivera had calculated the resonant frequency of the optical fiber extending over the fast bimorph to be 1 kHz. When applying voltage across the fast bimorph, the largest fiber deflection was achieved at a resonant frequency of 0.597 kHz and 1.48 kHz for scanners A and B respectively. During the testing of scanner B, the fibers were unintentionally pulled off and later re-attached. This adjustment shortened the free hanging length of the fiber. Because the resonant frequency depends inversely on the square of the overhang length of the fiber, it follows that scanner B's fiber will have a higher than expected resonant frequency.

Conclusions and Future Work

The goal of the project was achieved: two functional piezo scanners were built, their mechanical properties analyzed, and the thermal dissipation from eddy currents analytically evaluated.

Further optimization and improved modeling is necessary to match the measured values of the fibers' deflections and resonant frequencies with the calculated values. A possible scanner improvement involves implementing larger bimorphs. Thicker bimorphs will increase the

strength and durability of the scanners; longer bimorphs will allow for larger deflections of the fiber thereby providing a larger field of view.

Upon reaching the desired deflections and resonant frequencies, the next step in developing COMPMRI's piezo scanner is testing it in a magnetic field similar to that of an MRI machine.

As the other components of the COMPMRI system are additionally improved, testing of the system on animal subjects will follow. With further development, the COMPMRI system, with its *in vivo*, through-skull imaging capabilities, will eventually be implemented in research on brain functions and disorders.

Acknowledgements

This work was supported in part by the Cornell Center for Materials Research with funding from the Research Experience for Undergraduates program NSF grant (DMR-1460428 and DMR-1120296).

References

- [1] Wang K, Horton NG, Xu C. Going Deep: Brain Imaging with Multi-Photon Microscopy. Optics & Photonics News. November 2013.
- [2] Rivera DR, Brown CM, Ouzounov DG, et al. Multifocal multiphoton endoscope. Optics Letters. 2012;37(8).
- [3] Rivera DR, Brown CM, Ouzounov DG, et al. Compact and flexible raster scanning multiphoton endoscope capable of imaging unstained tissue. 2011;108(43).
- [4] Siakavellas NJ. Two Simple Models for Analytical Calculation of Eddy Currents in Thin Conducting Plates. IEEE Transactions on Magnetics. 1997;33(3).